THERMO-MECHANICAL BEHAVIOR OF A GRANODIORITE FROM THE LIQUIÑE FRACTURED GEOTHERMAL SYSTEM (39ºS) IN THE SOUTHERN VOLCANIC ZONE OF THE ANDES

J. Sepúlveda[a,b], G. Arancibia[a,b,c], E. Molina[a,b,c], J. P. Gilbert[d], M. Duda[d], J. Browning[a,b,e], T. Roquer[a,b], D. Morata[b,f], B. Ahrens[d], R. Bracke[d]

[a]Departamento de Ingeniería Estructural y Geotécnica, Pontificia Universidad Católica de Chile, Av. Vicuña Mackenna 4860, Macul, Santiago, Chile.

[b]Centro de Excelencia en Geotermia de los Andes (CEGA, FONDAP-CONICYT), Universidad de Chile, Plaza Ercilla 803, Santiago, Chile.

[c]Centro de Investigación en Nanotecnología y Materiales Avanzados (CIEN-UC), Pontificia Universidad Católica de Chile, Avda. Vicuña Mackenna 4860, Santiago, Chile.

[d]Institute for Geology, Mineralogy, and Geophysics, Ruhr-Universität Bochum, 44780 Bochum, Germany

[e]Departamento de Ingeniería de Minería, Pontificia Universidad Católica de Chile, Av. Vicuña Mackenna 4860, Macul, Santiago, Chile.

[f]Department of Geology, Facultad de Ciencias físicas y matemáticas, Universidad de Chile, Plaza Ercilla 803, Santiago, Chile

*Corresponding author: Gloria Arancibia (garancibia@ing.puc.cl)

Abstract: Fractures and faults in granitic rocks play an important role in geothermal systems because they permit the circulation of hot fluids. However, the thermo-hydro-mechanical behavior of granitic rocks has predominantly been studied at temperatures exceeding 300 °C and many geothermal systems experience temperatures much lower than this. The aim of this study was to evaluate how the depth, temperature, and amount and rate of mechanical loading associated conditions realistic in a low temperature geothermal system influence the physical properties of geothermal reservoir hosting rock. We carried out both room temperature and low temperature thermo-mechanical tests on a granodiorite sample from the Liquiñe area, Chile, and performed post-experimental x-ray microtomography analysis to numerically estimate the permeability of the generated fractures. The results showed that both rock strength and rock stiffness decreased with increments of temperature treatment related to the development of thermal crack damage at temperatures > 150 °C and through the development of sub-critical cracking at constant temperatures between 50 °C to 75 °C. Slowest deformed samples also exhibited lower strengths, attributed to the development of sub-critical cracking. The cyclic triaxial loading test indicated that significant mechanical fracture damage was only initiated above 80 % of the peak stress regardless of the number of repeated loading cycles at lower stresses. Low-temperature treatment appears to be a conditioning factor, but not the dominant factor in controlling the physical properties of reservoir hosting rocks. Our findings indicate that thermal crack damage is likely important for developing microfracture related permeability at depths of between around 2 to 6 km where the temperature is sufficiently high to induce thermal cracking. At shallower depths, such was previously estimated the reservoir of Liquiñe, thermal crack damage is only generated adjacent to fractures that remain open and circulate the hot fluids but sub-critical cracking over time reduces the strength of rocks in lower temperature regimes. These processes combined to produce a geothermal reservoir in Liquiñe which likely first required the presence of a highly fracture fault zone.

Key words: crystalline rock; thermo-mechanical properties; hydro-mechanical properties; fractured geothermal system; Andean Southern Volcanic Zone.

1 INTRODUCTION

The mechanical, thermal and hydraulic behavior of granitoids have been extensively studied because these rocks commonly represent the host rocks for a range of applications such as nuclear waste disposal (Zhao, 2016), underground coal gasification (Gautam et al., 2018), building construction (Vázquez et al., 2015; Vazquez et al., 2018) and enhanced geothermal systems (Géraud et al., 2011, Shao et al., 2015; Yang et al., 2017).

Granitoid permeability is conditioned by the presence of interacting fractures and faults that form interconnected networks which can in turn be accessed by fluids (Sibson, 1996). The spatial distribution, geometry and density of fractures creating these networks are influenced by intrinsic properties of the rock mass such as mineralogy and textures, and external factors such as burial depth, temperature, stress field and the degree of pre-existing fracturing or faulting. In order to understand the thermo-mechanical behavior of granitoids of different intrinsic properties and under different external conditions, several experimental approaches have been carried out on a range of rock types and under different amounts of confining pressure, pore-fluid pressure and temperature (e.g. Meredith and Atkinson, 1985; Dwivedi et al., 2008; Yang et al., 2017).

Studies have shown that fracture propagation can also be characterized and determined through the *stress intensity factor* K_I (in mode I fractures), where propagation occurs when the critical value K_{IC}, which corresponds to *fracture toughness*, is reached. K_{IC} describes the resistance to dynamic fracture propagation (Brantut et al., 2013) but it is known that fractures can propagate at stress states lower than K_{IC} through processes of sub-critical crack growth. This is a time dependent process and is influenced by external factors such as the level of stress intensity, temperature, depth and pressure, and microstructure and residual strain (Atkinson, 1984).

Furthermore, mechanical tests under different external conditions have shown that the strength of a rock is dependent on the rate at which it is deformed (Blanton, 1981; Kumar, 1968; Lajtai et al., 1991; Duda & Renner, 2013). Some explanations for this observation are that lower strain rates produce dominantly intragranular cracking, and the mechanism of cracking changes to transgranular or grain boundary cracks at higher strain rates. The result of this changing crack growth mechanism is that rocks appear stronger at higher strain rates (Liang et al., 2015). Additionally, time-dependent microfailure processes such as subcritical crack growth affect the bulk mechanical behavior more significantly at lower strain rates than at higher strain rates (Atkinson, 1984; Brantut et al., 2013). As a consequence, strength generally increases with increasing strain rate, but the strain-rate dependence of strength decreases with increasing confinement (Hokka et al., 2016). In geothermal settings this is important because most granitoids presumably reside in the crust at a critically stressed level and normally experience slow strain rates. However, when a fault slips forming an earthquake, the strain rate can locally increase by several orders of magnitude.

Stress paths in faults regions and natural geothermal systems are inherently cyclic. In cases where the loading stress remains below the strength of the rock, microstructural damage is generated instead of bulk rock failure (Mitchell & Faulkner, 2008; Heap et al., 2013). Cyclic stress paths have been well-studied in the laboratory by monitoring both the output of acoustic emissions (AE) and the evolution of strain during cyclic loading tests (e.g. Lockner, 1993; Browning et al., 2017). It has been found that rocks exhibit a *Kaiser stress memory effect,* meaning that the rock only produces significant evidence of inelastic crack growth (e.g. output of AE or deviation of volumetric strain from a linear compacting trend) when the previous maximum stress state has been reached or exceeded (Zhu & Wong, 1997; Heap et al., 2009; Browning et al., 2018). As such, any loading up to the previous maximum stress is effectively elastic and that portion of deformation effectively grows larger with increased stress cycling. However, it has been noted that the Kaiser effect is not as pronounced when the rate of deformation is high (Lavrov, 2001).

Cyclic loading tests indicate that stress cycling can also produce changes in the mechanical properties of rocks, but such changes only occur right upon the initiation or onset of microfracturing (Brace & Byerlee, 1966; Kumar, 1968; Heap et al., 2009). Microfractures nucleate and grow when the level of differential stress exceeds some critical value regardless of the level of mean stress (Browning et al., 2017). The newly formed fractures generate an anisotropy aligned perpendicular to the direction of the minimum principal compressive stress. The new fracture damage produces permanent changes to the physical rock properties which can be discerned from ultrasonic wave velocity measurements (Browning et al., 2017; Passelègue et al., 2018).

An additional external factor that produces changes in the behavior of the rocks is the amount of applied confining pressure, as an equivalent of the burial depth, which has been commonly observed to increase both rock strength and stiffness. This is because fractures tend to close when they are exposed to greater levels of confining pressure (e.g. Yang et al., 2017), and as a consequence, permeability correlates inversely with this factor (e.g. David et al., 1999). When a confining pressure is applied fractures tends to close but will reopen when a sufficient and preferentially oriented differential stress or pore fluid pressure are applied even at confining pressure of 130 MPa (Violay et al., 2017).

Furthermore, microfractures will nucleate when the level of differential stress exceeds the elastic limit and the permeability then increases (Chen et al., 2014; Nara et al., 2011).

As well as mechanical loading, changes in temperature (or thermal loading) of rock volume induce thermal stresses which can lead thermal cracks in rocks and change the physical rock properties (e.g. Hommand-Etenne & Houpert, 1984; Moore et al., 1994; David et al., 1999; Huang et al., 2017; Griffiths et al., 2017; Castagna et al., 2018). The distribution and amount of thermal cracks are a consequence of both heating and mineral expansion as well as cooling and mineral contraction (Browning et al., 2016). The effect of thermally induced damage on the bulk properties of the rock volume depends on the temperature that the rock reached, a variable which can be qualitatively estimated by the change in mechanical rock properties (Guo et al., 2017; Kumari et al., 2017), but which is also controlled by the mineralogical composition of the rock. For example, when a brittle intrusive rock is heated to temperatures between 100-300 ºC the change in strength and stiffness are thought to decrease only marginally, and thermally induced stresses are small compared to confining pressures typically associated with such reservoir temperatures (Kumari et al., 2017). The effect of temperature on the rock-physical properties becomes more pronounced at higher temperatures, for example beyond 573 ºC for many rocks, when the amount of thermal damage increases exponentially with temperature because of the anisotropic expansion of the $\boxed{\alpha/\beta}$ quartz transformation (Glover et al., 1995; Ohno, 1995; Meredith et al., 2001; Ohno et al., 2006).

The vast majority of previous studies on the effects of thermal cracking focused on the effects of higher temperatures stressing over the range of 300 ºC to 1000 ºC, and a few studies have reported the behavior of granitic rock at temperatures below 300 ºC (Chen et al., 2017; Kumari et al., 2017; Molina et al., 2019). In a low enthalpy geothermal system, fluids circulate at low temperatures between 50 and 200 ºC, and even small thermally induced stresses may strongly affect its hydraulic properties. For example, it has been found that at heating rates as low as 1 ºC/min, and at temperatures of 80 ºC thermal stressing is enough to generate thermal cracks in granites (Griffiths et al., 2018).

In Chile, the expected geothermal potential is immense. For example, Lahsen et al. (2010) estimated the geothermal power capacity at around 3350 MW and Aravena et al. (2016) estimated an electric potential of about 650 MWe. These estimates were based on the area from 17-28 ºS (known as Central Volcanic Zone, CVZ) and between 36 and 46ºC (Southern Volcanic Zone, SVZ) which is evidenced by the presence of numerous active volcanoes. Liquiñe (39 ºS, SVZ) represents an area in Chile where different active faults systems cut intrusive rocks corresponding to the North Patagonian Batholith (NPB). Moreover, numerous hot springs with temperatures between 40 ºC and 70 ºC outcrop above the NPB and are spatially related to the main fault systems (Sánchez et al., 2013).

Understanding the circulation of fluids pathways through faults and fractures in the potential Liquiñe geothermal reservoir is important to further constrain the conditions that allow fluid circulation. Therefore, the aim of this study is to estimate how a low to medium enthalpy geothermal reservoir (< 250 ºC) is affected by fractures generated by both mechanical and thermal stressing under dry conditions. This is relevant because such conditions likely influence the development of permeability related to fractured geothermal systems associated to the faults present in the area. We sampled cores from a representative intrusive rock outcrop named "La Cantera", measured the hydraulic and dynamic properties before we thermally and mechanically stressed the samples and repeated the measurements. A suite of thermo-mechanical tests were therefore performed and x-ray microtomography images were taken on the deformed samples in order to numerically estimate fracture permeability. The present work represents a laboratory approach to understand the behavior of this granodiorite as a potential host rock of this geothermal reservoir, given the absence of direct information via boreholes or results of previous investigations of the host rock in the area like other authors have performed (i.e Brantut et al., 2017). We performed a range of laboratory tests to understand the mechanical and hydraulic behavior of this rock at depth and modelled the permeability of fractures to characterize the potential fluid pathways.

2 GEOLOGICAL SETTING OF CASE STUDY

The Southern Volcanic Zone (SVZ) is an active magmatic zone, where the tectonics are controlled by oblique subduction between the Nazca and South American plates, producing a tectonic setting where deformation is partitioned into margin-parallel and margin-orthogonal faults, accommodated within the arc and fore-arc, respectively (e.g. Arancibia et al., 1999; Cembrano et al., 1996; Stanton-Yonge et al., 2016) (Fig. 1a). The basement of the volcanic arc in the SVZ corresponds to the North Patagonian Batholith (NPB) conformed by tonalitic to granodioritic Jurassic – Miocene rocks which have accommodated at least 500 km of extension (Munizaga et al., 1988; Pankhurst et al., 1992; Pankhurst et al., 1999). The NPB is cut by the Liquiñe-Ofqui Fault System (LOFS) (and the Andean Transverse Faults (ATF; Cembrano & Hervé, 1993; Hervé et al., 1993; Cembrano et al., 1996; Arancibia et al., 1999; Rossenau et al., 2006; Cembrano & Lara, 2009; Pérez-Flores et al., 2016).

The LOFS (38-47 ºS) is an active intra-arc, trench-parallel fault system produced by the partitioning of intraplate deformation. This system is 1200 km long, with dextral and dextral-normal faults that strike NS-NNE to NE-ENE, respectively (Cembrano et al., 1996; Arancibia et al., 1999; Cembrano & Lara, 2009). The LOFS oblique slip rates range between 1 and 7 mm/year during the inter-seismic phase of a subduction seismic cycle (Stanton-Yonge et al., 2016). The ATF include a group of active NW-striking sinistral faults and morphotectonic lineaments. The faults of the ATF have a variable length ranging between approximately 10 to 20 km (e.g. Rossenau et al., 2006; Melnick et al., 2006; Cembrano & Lara, 2009; Pérez-Flores et al., 2016). These faults are misoriented with respect to the regional stress regime and during the inter-seismic phases of the subduction seismic cycle they accommodate a maximum oblique slip of 1.4 mm/year (Stanton-Yonge et al., 2016).

In the Liquiñe area (Fig. 1b) the Paleozoic metamorphic rocks were intruded by the NPB which is composed of tonalites, diorites and granodiorites of Jurassic, Cretaceous and Miocene ages (Lara & Moreno, 2004). Additionally, volcanic and volcanoclastic rocks cover the area and are related to the eruptions of the nearby volcanoes (Villarrica-Quetrupillán-Lanín and Mocho-Choshuenco) and minor eruptive centers. Quaternary fluvial, colluvial and moraine sedimentary deposits also drape the area. Finally, several thermal springs are located within the fractured crystalline rocks (Fig. 1b).

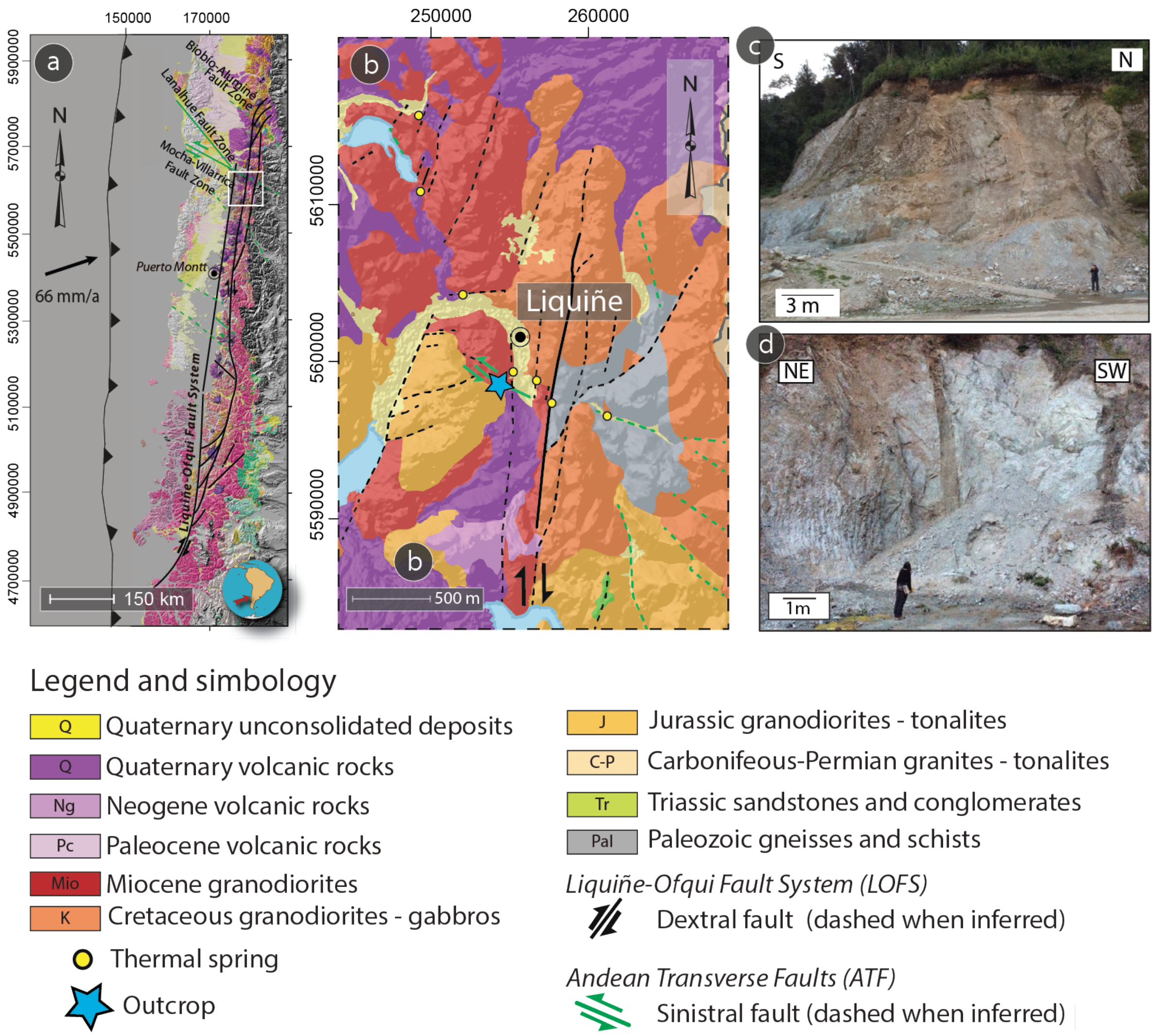

Figure 1. a) Regional map of the Southern Volcanic Zone. Oblique subduction between Nazca and South American plates occurs with rate of 6 mm/a (Angermann et al., 1999). The black and green lines correspond to the Liquiñe-Ofqui Fault System and Andean Transverse Faults, respectively. The white square indicates the area of the study case Liquiñe covered by b). b) Liquiñe geological map where the selected outcrop, "La Cantera", is indicated by a light blue star. A general view (c) and a zoom (d) of the outcrop. Modified after Lara & Moreno (2004), Sánchez et al. (2013), and Pérez-Flores et al. (2017).

3 EXPERIMENTAL MATERIALS AND METHODOLOGY

3.1 Material and samples preparation

A well exposed and representative outcrop of the Liquiñe area, "La Cantera" (Fig. 1c and 1d), was selected to extract two adjacent blocks of the Miocene granodiorite documenting their relative orientation to each other. On a macroscopic scale, the granodiorite shows medium-sized grains of quartz, feldspar, plagioclase, opaque minerals and biotite altered to chlorite. The outcrop showed several faults, fractures, dikes, and milli- to centimeter veins of chlorite and epidote but we were careful to select samples which not obviously exhibited such features.

Figure 2 shows microphotographs of thin section of the granodiorite investigated in this study. The modal composition and textures were determined using a Leica DM750P polarized optical microscope (POM) equipped with a digital microphotography unit model Leica EC3. The sample exhibits a phaneritic texture with a grain size that varies between 0.3 mm and 5 mm, and the rock is composed by quartz (25 %), plagioclase (37 %), k-feldspar (18 %), biotite (15 %), amphibole (2 %) and opaque minerals (3 %) (Fig. 2 a and b). The biotite is altered to chlorite, and the k-feldspar and plagioclases are altered to sericite, epidote and calcite. We also observed textures such as granophyric quartz and k-feldspar, perthitic k-feldspar and zoned plagioclase. The sample is cut by veins of between 0.05 to 0.2 mm thick mainly filled with epidote and, secondarily by chlorite (Fig. 2 c).

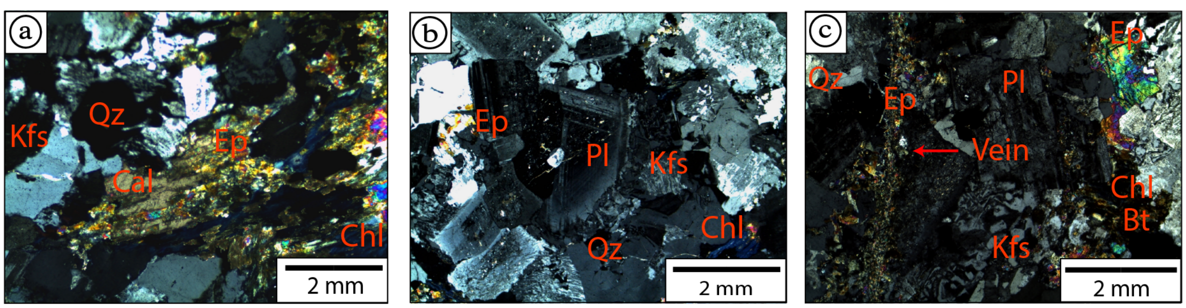

Figure 2. Optical microphotographies (crossed nicols) of natural granodiorite sample. a) and b) highlights the bulk mineralogy; whereas c) shows a vein of epidote pointed by a red arrow. Legend: Qz: quartz, Ep: epidote, kfs: k-feldspar, Pl: plagioclase, Bt: biotite, Chl: chlorite, Cal: calcite.

3.2 Thermal stressing

In order to understand how temperature influences the physical properties of the host rock from the Liquiñe Geothermal System,15 samples were cored, in the same orientation, from the two granodiorite blocks, with diameters of 55 mm and lengths of 110 mm. All of the samples were ground flat and parallel. Of the samples, five were heated for six hours in an oven at 150 ºC and another 5 were heated at 210 ºC, both sets were heated at atmospheric pressure and the temperature was applied with a heating rate of 6 ºC/min. After these six hours, samples were cooled very slowly inside the oven until the reach the room temperature. The remaining five samples were not heat-treated to serve as a reference. Because all of the samples were dried at 70 ºC, we refer to those samples dried at 70 ºC, and without other thermal treatment, as 'without thermal treatment' or from now on, as 'as-received'. We were careful to check that the 70 ºC drying did not induce any significant changes in the physical rock properties.

3.3 Field Emission Scanning Electron Microscope (FESEM)

Three polished thin sections were prepared to describe the original 'as received' material and any changes in micro-structure produced by the thermal treatment at the two different temperature, by using a Quanta FEG 250, from FEI Technologies Inc. (acceleration voltage of 25 kV). The sample surfaces need to be coated with a conductive layer of gold (5.0 ± 0.1 nm of thickness), with a Sputter Coater Cressington 108, before FESEM scanning to improve the resolution of the images. FESEM equipment is located at Centro de Investigación en Nanotecnología y Materiales Avanzados (CIEN-UC), Pontificia Universidad Católica de Chile.

3.4 Physical properties

Grain density $\boxed{\rho_{\mathrm{grain}}}$ was gained from pycnometer measurements on crushed and ground sample powder following the normative UNE-EN 1936 (2007):

$$\boxed{\rho_{\mathrm{grain}} = \frac{m_{\mathrm{d}}}{m_{\mathrm{s}} - m_{\mathrm{h}}} * \rho_{\mathrm{wat}}} \qquad \text{(Eq. 1)}$$

Here, $\boxed{m_{\mathrm{d}}}$, $\boxed{m_{\mathrm{s}}}$, and $\boxed{m_{\mathrm{h}}}$ denote the masses of the dried, saturated, and submerged sample powder in distilled water in kg. The density of distilled water at 20 °C is referred to as $\boxed{\rho_{\mathrm{wat}}}$ (in kg/m^3), and the powder was milled from a fragment of a block.

To evaluate the amount of thermal damage generated by thermal treatment of the samples, we measured porosity, ultrasonic wave velocities and water absorption before and after each thermal treatment. The total and effective porosities, Φ_{tot} (in %) and Φ_{eff} (in %), were measured following the norm UNE- EN 1936 (2007) according to:

$$\Phi_{\mathrm{tot}} = \left(1 - \frac{\rho_{\mathrm{geo}}}{\rho_{\mathrm{grain}}}\right) * 100 \quad \text{(Eq. 2)}$$

$$\Phi_{\mathrm{eff}} = \left(\frac{m_{\mathrm{s}} - m_{\mathrm{d}}}{\rho_{\mathrm{wat}} * V_{\mathrm{geo}}}\right) * 100 \quad \text{(Eq. 3)}$$

Where ρ_{geo} and V_{geo} correspond to the geometric density (in kg/m^3) and volume (in m^3), respectively.

The capillarity coefficient C_C was measured after oven-drying the samples at 70 ºC for 24 h and then leaving to cool for an additional 24 h. The samples were carefully lined around their edges with an impermeable tape and the open bottom face was immersed in water to a depth of 3 ±1 mm. A porous spacer was used to guarantee a spatially uniform fluid flow into the samples. Finally, the mass of the samples $m_s(t)$ was measured at different times t following the norm UNE-EN 1925 (1996) and C_C was calculated according to

$$C_{\mathrm{c}}(t) = \frac{m_s(t) - m_d}{A\sqrt{t}}, \quad \text{(Eq. 4)}$$

where A denotes the cross-sectional area of the sample.

Ultrasonic compressional (V_P [m/s]) and shear wave velocities (V_S [m/s]), were measured in dried samples, before and after heat-treatment, using a 54 kHz polarized PROCEQ transducers (P/N325) for P-waves and 500 kHz Olympus transducers V150-RB for S-waves, with a contact surface diameter of 4 and 3.5 cm, respectively, in according with ASTM D2485 (2005). An ultrasound gel was used to ensure a good coupling between the sample surfaces and transducers. The transducers were placed on the top and the bottom of the sample and were fixed with plastic pieces and a small constant axial stress of 0.2 MPa was applied by a pneumatic piston. We calculated dynamic Young's modulus E_d (in MPa), bulk modulus K_d (in MPa) and Poisson's ratio ν_d according to the norm ASTM D2485 (2005):

$$\boxed{E_d = \frac{[\rho\, V_s^2(3V_p^2 - 4V_s^2)]}{V_p^2 - V_s^2}} \quad \text{(Eq. 5)}$$

$$\boxed{K_d = \frac{\rho\left(3V_p^2 - 4V_s^2\right)}{3}} \quad \text{(Eq. 6)}$$

$$\boxed{\nu_d = \frac{V_p^2 - 2V_s^2}{\left[2\left(V_p^2 - V_s^2\right)\right]}} \quad \text{(Eq. 7)}$$

3.5 Mechanical characterization

Conventional uniaxial and triaxial compression tests were performed on both the 'as received' and thermally treated samples in order to characterize the mechanical behavior of the rocks under elevated pressure but under room temperature conditions. All mechanical tests were performed under dry conditions and following the norm ASTM D702-14 (2010). For these experiments three uniaxial tests and three conventional triaxial tests (at constant confining pressures p_c of 10 MPa) were performed on both the as-received and the thermally treated samples at a hydrostatic loading rate of 1 MPa/s, with a precision of ± 5%. The tests were carried out in the Geotechnical Laboratory at Pontificia Universidad Católica de Chile with a 50-C5632 Controls Uniaxial press (Fig. 3a). The confining pressure was generated using a Hoek cell and a hydraulic oil pump to create the necessary confining pressure with an accuracy of ± 1%. Axial and radial strain was measured with two axial and radial strain gauges (PFL 20-11), and the accuracy of the strain measurements was ± 2%.

In order to understand the effect on the mechanical behavior of the rocks under different strain rates and deformed at elevated temperatures, a suite of nine triaxial experiments were performed using a thermo-triaxial hydraulic press at the International Geothermal Centre in Bochum (GZB), Germany (Fig. 3b). Thermo-triaxial deformation experiments were conducted on samples (length: 100 mm, diameter: 40 mm) at three different temperatures of room temperature, 50 ºC and 75 °C, and three different strain rates of 10^{-3}, 10^{-5}, and 10^{-7} s^{-1}. All of the tests were performed at a confining pressure of 25 MPa. The samples were jacketed with Viton sleeves to prevent the confining medium from penetrating the sample. Axial load was applied using a servo-controlled double acting hydraulic actuator using external inductive displacement transducers. Confining pressure was applied by a servo-controlled double acting pressure intensifier and hydraulic oil was used as the confining medium. Temperature was measured using one thermocouple located at a central point within the pressure vessel (Fig. 3b). Axial load and radial strain were measured with an external load cell and a circumferential measurement system consisting of a radial chain and a displacement transducer. Axial strain was determined by correcting the loading piston displacement for system characteristics as derived from calibration experiments on a hardened steel sample. Once the test was finished the samples were axially unloaded in step and at the rate of ~10^{-5} s^{-1} stress load and then the confining pressure was reduced at 1 MPa/s at rate of ~ 0.15 MPa/s.

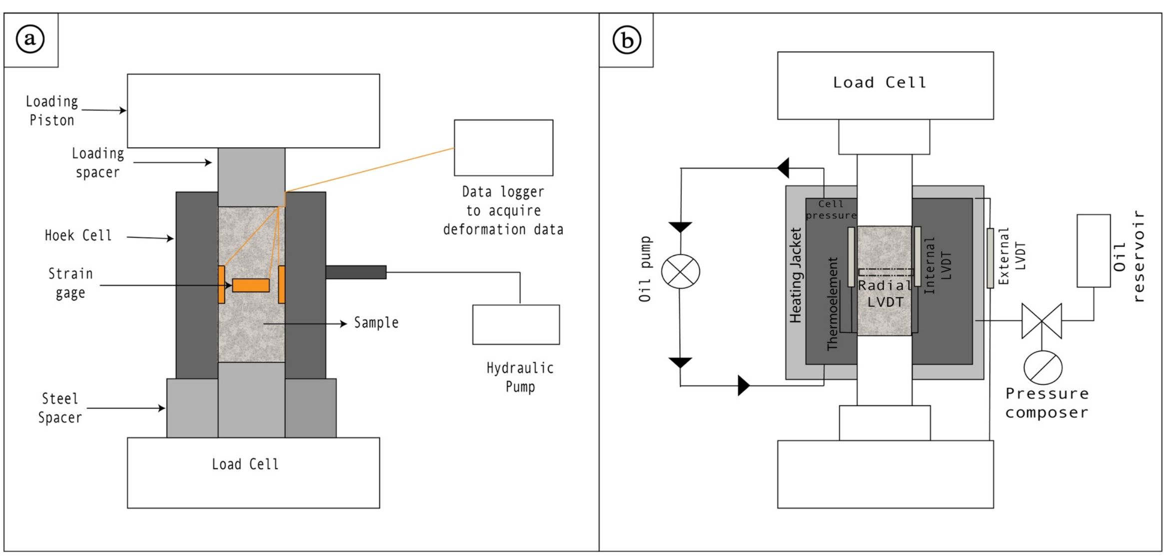

Figure 3. a) Scheme of the triaxial apparatus at Pontificia Universidad Católica de Chile; b) Scheme of the triaxial apparatus at the International Geothermal Centre.

In addition to altered strain rate and elevated temperature tests, one cyclic triaxial loading test was carried out at GZB. For this, one sample was cyclically loaded to repeated peaks of 60%, 70% and 80% of the failure stress as estimated by the conventional triaxial deformation at comparable experimental conditions, that is, 25 MPa confining pressure, room temperature and an imposed strain rate of 10^{-5} s^{-1}. After each cycle, the samples were unloaded to initial hydrostatic conditions. Following axial loading up to 80 % of the failure stress, axial stresses were decreased to 60% of the failure stress to try to understand the effect of incomplete unloading.

3.6 X-Ray Micro Computerized Tomography and Permeability Modelling

X-ray micro computerized tomography is a non-destructive technique that allows the observation of the internal structure of materials determined by differences in the atomic composition of each compound (Mess, 2003). This technique has been used in geoscience and engineering to solve many different types of scientific problem (Cnudde & Boone, 2013). One of the most recent problems is the quantitative characterization of pore and fracture volumes and geometries from high resolution images to understand pore-scale processes governing rock properties (Andrä et al., 2013).

In this study, four samples were scanned at GZB following their deformation in the thermal triaxial tests to understand the effect of temperature, strain rate and cyclic loading on macro-fracture development. The four samples selected for scanning were those deformed at room temperature and 75 ºC at 10^{-3} s^{-1} of strain rate and, at room temperature and a strain rate of 10^{-7} s^{-1}, and the sample cyclically loaded at room temperature and a strain rate of 10^{-5} s^{-1}.

The images were processed in the open source software *ImageJ* (Schindelin et al., 2012; Schneider et al., 2012) (https://imagej.net/) and an anisotropic diffusion filter (Tschumperlé & Deriche, 2005) was applied to remove the noise and improve the quality. The solid and porous volumes were segmented using a threshold grey value. Thereafter, *BoneJ* plugin (Doube et al., 2010) was applied to measure the aperture of fractures through a volume of 466x466x750 pixel. The resolution of fractures was limited by the resolution of the scans with a pixel dimension of 55.43 μm.

In this study, permeability (*k*) was numerically calculated in order to understand the interaction between fluids and the host rock with the assumption of constant fluid flux. Permeability was estimated from measurement of the void space and simulation of fluid flow through the fractures using the Lattice-Boltzmann method with the Parallel Lattice Boltzmann Solver software (Palabos, www.palabos.org) (Anissofira & Latief, 2015; Latief & Fauzi, 2012) in a D3Q19 scheme. This parameter was calculated following the axial direction, parallel to the applied differential stress and hence it was assumed that fractures would grow parallel to the sample axis. Equation 8 is a modification of Darcy's Law designed to conform with the Palabos software such that:

$$k = \frac{\mu \langle v \rangle}{dP/dL} \quad \text{(Eq. 8)}$$

Where $\mu \langle v \rangle$ is the mean fluid flow velocity through the fractured media, ΔP is the pressure gradient between the top and bottom of the sample to generate the flow (ΔP = 0.00005) and ΔL is the length of the sample. Finally, to visualize the 3D images and hence characterize the fracture and permeability measurements we used the open software Paraview (Ahrens et al., 2005) (www.paraview.org).

3.7 Hydrostatic permeability methods

Prior to deformation we measured the permeability of three saturated, as received, samples to estimate the change in permeability with confining pressure. All of the samples were prepared with 30 mm in diameter and 80 mm in length and measurements were taken at confining pressures of 10 MPa, 15 MPa and 25 MPa and at room temperature. The measurements were performed in a Hoek Cell at *Ruhr-Universität Bochum.* Distilled water was pumped through the sample at 0.001 ml/min and permeability was calculated using the steady-state flow method from a modification of Equation 8 following:

$$k = \frac{\Delta V * \mu * L}{P * A} \quad \text{(Eq. 9)},$$

Where k is the permeability (in m^2), μ is the viscosity of the fluid (0.001 Pa s), L is the length of the sample (in m), P is the pressure gradient (in Pa), A is the cross sectional area of the sample (in m^2), and ΔV is the gradient of the change in water volume (in m^3/s).

4 RESULTS

4.1 Effect of thermal stressing on physical properties

4.1.1 Sample description from FESEM

In Figure 4 we present a serie of images from FESEM scans that allow a comparison of the relative amounts of thermal damage produced from each thermal stressing treatment. The presence of a small number of pre-existing intergranular fractures within plagioclase, k-feldspar and quartz can be observed, which are presumably either a product of the natural cooling of the rock during emplacement or tectonic stressing. In samples heated at 150 ºC we note the presence of a greater number of transgranular or grain boundary fractures and larger fractures. In samples heated to 210 ºC, the number of transgranular fractures grows substantially, the shape is more tortuous and deeper than the other cases. Grain boundary fractures occurred mainly at the interface between plagioclase and k-feldspar crystals. In samples heated at 150 ºC and at 210 ºC is possible to observe that fractures are surround dense minerals, but the fractures do not cut the mineral. In the three cases we noted a network of fractures that are connected between them, but these networks are essentially determined by the grain shape.

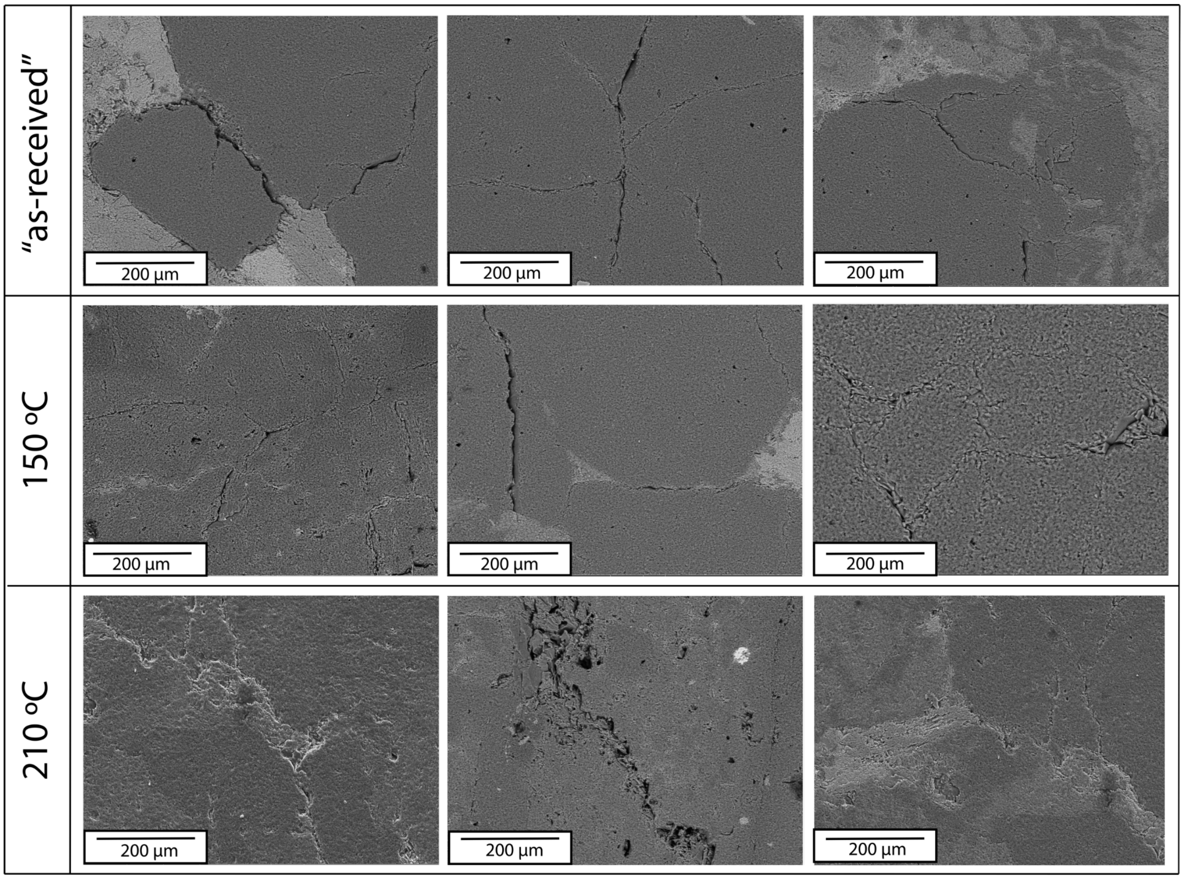

Figure 4. FESEM microphotographies showing the pre-existing intergranular fractures in the as-received sample and the more abundant fractures in the thermally stressed samples at 150 ºC and 210 ºC.

4.1.2 Physical properties and ultrasonic wave velocity measurements

The mean density (ρ_r) at room temperature and in as received samples was 2669 kg/m^3. The average of total porosity (Φ_{tot}), effective porosity (Φ_{eff}), capillarity coefficient (C_c) for each group of 5 samples are indicated in Table 1, all the measurements, except C_c were performed under dry conditions. The porosities and the measured density in the as received rock were within the typical range of granodiorites from elsewhere (Vazquez et al., 2018). In comparison to the as-received samples, the effect of thermal treatment to 150 ºC produced a decreased in Φ_{tot} and Φ_{eff} of 3.6% and 2.4%, respectively, and an increment of Cc to 12.2%. In samples treated to 210 ºC, the reduction of Φ_{tot} and Φ_{eff} was 14.3% and

24.6%, but C_c increased to 22.7%. In both cases, Cc increased but the porosities (Φ_{tot} and Φ_{eff}) decreased with increments of temperature.

T	ϕ_{tot}	ϕ_{eff}	Cc	V_P	V_S	E_d	ν_d	K_d
	Mean ± St. D.	Mean ± St. D.	Mean ± St. D.	Mean ± St. D.	Mean ± St. D.	Mean ± St. D.	Mean ± St. D.	Mean ± St. D.
as-received	2.2 ± 0.3	1.5 ± 0.2	1.7 ± 1.0	4605± 322	2544±45	44 ± 4.4	0.28 ± 0.05	34 ± 7.6
150	2.1 ± 0.2	1.5 ± 0.2	1.9 ± 0.9	4636± 79	2853± 43	52 ± 1.5	0.19 ± 0.02	28 ± 1.6
210	1.9 ± 0.2	1.2 ± 0.2	2.1 ± 0.5	4128± 250	2544± 55	41 ± 5	0.19 ± 0.01	23 ± 2.9

Table 1. Physical properties of as-received and heat-treated samples and their variation with respect to their initial values, averaged over five measurements. T: temperature (°C); St. D.: standard deviation; Φ_{tot}: total porosity (in %); Φ_{eff}: effective porosity (in %); C_C: capillarity coefficient (in g m^{-2} $s^{-0.5}$); V_p: P-wave velocity (in m/s); V_s: S-wave velocity (in m/s); E_d: dynamic young modulus (in GPa); ν_d: dynamic Poisson's coefficient; K_d: dynamic bulk modulus (in GPa).

The compressional wave velocities (V_p) (Table 1) recorded in samples heated to 150 ºC increased by 0.68% in relation to the as-received samples, whereas the increase in V_s for the same respective samples was 12.14%. Samples heated to 210 ºC, conversely, produced a decrease in V_p of 10.36% compared to the as received samples. However, the V_s did not change significantly with respect to measurements on the as received samples.

The dynamic elastic moduli (E_d), derived from the ultrasonic wave velocity measurements, also changed following thermal treatment in all of the samples. Dynamic Young's moduli decreased from 44 GPa in the as received samples to 41 GPa in the samples heated to 210 ºC, a decrease of 6.1 %. The Poisson's coefficient and bulk modulus (ν_d and K_d), of samples heated to 210 ºC, also decreased by 29.8% and 33.3%, respectively, in relation to the as received samples. However, the samples heater to 150 ºC showed an increase of 17.9% in the E_d, but a decrease in both ν_d and K_d of 29.2% and 15.8%, respectively.

4.1.3 Uniaxial and triaxial deformation tests

In Figure 5 we report the axial differential stress against both volumetric and axial strain under uniaxial conditions. It can be seen that the stress-strain curves and peak stress at failure were similar in tests conducted on both the as-received sample and the sample heated to 150 ºC. However, the test performed on the sample heated to 210 ºC showed that the strain for any given stress was larger than in the previous samples (Fig. 5a). When a confining pressure of 10 MPa was applied in the triaxial tests (Fig. 5b), we noted that the stress-strain curves for the as-received samples were more similar to those of the sample heated to 210 ºC.

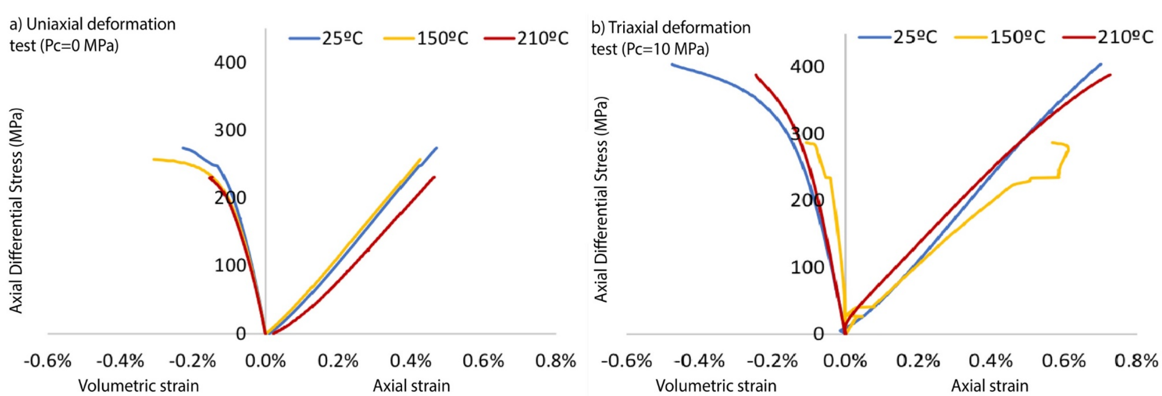

Figure 5. Axial differential stress vs both volumetric and axial strain curves in a uniaxial deformation test (a) and a triaxial deformation test at 10 MPa of confining pressure (b) of the samples heated at 150 ºC and 210 ºC (yellow and red curves) and of the as-received sample (blue curve). P_C: Confining pressure.

The results presented in Table 2 indicate that the peak stress or strength (σ_{max}) decreased by 16 MPa in the sample heated to 150 ºC and 43 MPa in the sample heated to 210 ºC with respect to the as received rock. A similar decrease was observed in the static Poisson's coefficient (ν_s), the static bulk modulus (K_s) and theYoung's modulus (E_s). The three static moduli maintained their values in samples heated to 150 °C with slight variations, but the biggest change was in the sample heated to 210 °C where the E_s and the K_s decreased by 8 GPa and 9 GPa, respectively, and the ν_{stat} was reduced by 0.07 from 0.18 to 0.11.

When a confining pressure equal to 10 MPa was applied, both the σ_{max} and the E_s were higher than as received sample and the sample heated to 210 ºC tested without confining pressure. In comparison to the unconfined tests, σ_{max} increased by 130 MPa in the test on the as-received sample, 158 MPa in the tests on the sample heated to 210 ºC but decreased by 22 MPa in the test conducted on the sample heated to 150 ºC, under confinement. Also, σ_{max} decreased by 168 MPa (210 ºC) and 15 MPa (150ºC) with respect to the as received samples. E_s did not change significantly in samples heated to 210 ºC the sample heated at 150 ºC experienced highly abnormal deformation behavior and the measured strength was much lower than the other samples (at 25 ºC and 210 ºC).

T	P_C	σ_{max}	Max. Axial strain	Max. Radial strain	E_s	ν_s	K_s
"as-received"	0	274	0.47	-0.001	56	0.18	29
150	0	258	0.43	-0.0002	54	0.18	28
210	0	231	0.47	-0.0016	46	0.11	20
"as-received"	10	404	0.7	-0.0007	60	0.24	38.4
150	10	236	0.61	-0.0001	51	0.1	21.1
210	10	389	0.72	-0.0005	58	0.21	33.5

Table 2. Results of the uniaxial deformation test (0 MPa) and triaxial deformation test (10 MPa), and static moduli. T: temperature of heating (in ºC); $P_{C:}$ confining pressure (in MPa); $\sigma_{max:}$ peak stress at failure (in MPa); Max. axial strain: maximum axial strain at maximum applied stress (in %); Max. radial strain: maximum radial strain at maximum applied stress (in %); E_s: static Young's modulus (in GPa); K_s: static bulk modulus (in GPa); ν_s: static Poisson's coefficient.

4.2 Triaxial tests at different strain rates and elevated constant temperature

Prior to the thermo-mechanical loading several rock properties for the used samples were measured before of the mechanical tests. The average rock sample density measured was 2626 ± 9 g/cm^3 and the total porosity was 0.8%. Additionally, the average measured V_P and V_S were 4983 ± 88 m/s and 2759 ± 126 m/s, respectively; and E_d, K_d and ν_d were 51.9 ± 3.5 GPa, 39.2±4 GPa and 0.28 ± 0.03, respectively. In Figure 6 the stress vs strain and stress vs time were plotted for the three tests at each strain rate and temperature tested. In the elastic portion of the loading cycle, in all tests, we observed similar stress and strain behavior, for any given strain rate regardless of the temperature that the test was performed at. However, we note marked strength decreases in the tests performed at elevated temperatures in all of the strain rates tested.

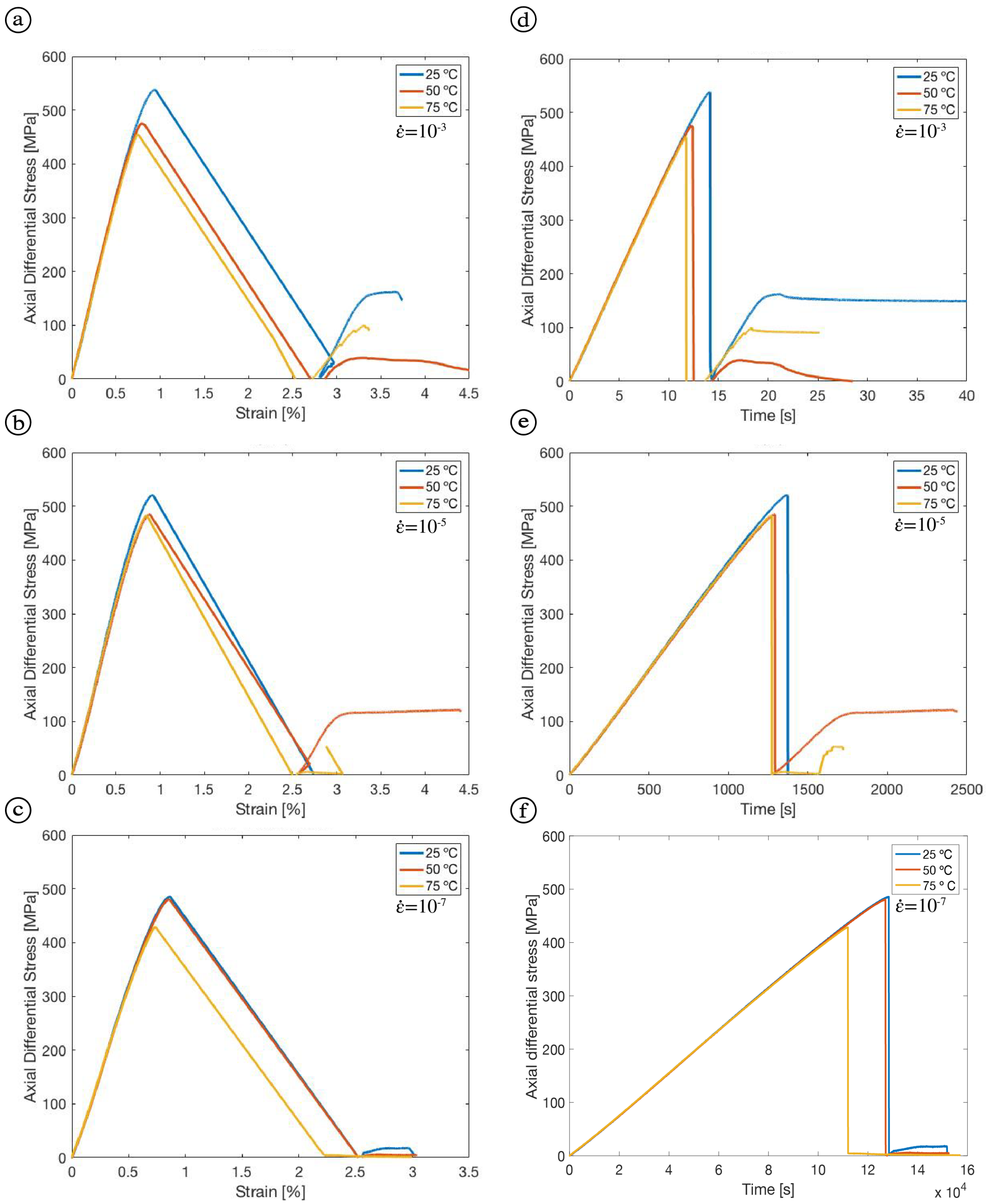

Figure 6. Axial Stress-strain and Stress-time curves at 25 MPa of confining pressure as a function of different strain rates and different temperatures. Graphics a, b and c give stress against strain for strain rates (ε) of 10^{-3} s^{-1}, 10^{-5} s^{-1} and 10^{-7} s^{-1}. Graphics d, e and f give axial stress against time for different strain rates.

In table 3 we report the data from the triaxial tests at elevated temperature and under different strain rates. A general observation was that strength increased with highest strain rates at almost all the temperatures tested, although with a slight exception at the highest temperature. The change was most notable in the tests at room temperature where the measured strength was 541 MPa in the fastest test but decreased to 520 MPa and 486 MPa in the two slower tests. The test performed at 50 ºC produced a decrease in strength of 14 MPa and 19 MPa at strain rates of 10^{-5} $s^{-1}$and 10^{-7} s^{-1}, with respect to the sample loaded at 10^{-3} s^{-1}. The test performed at 75 ºC produced the highest strength of 477 MPa at 10^{-5} s^{-1} which decreased to 457 MPa at a strain rate of 10^{-3} s^{-1} and 429 MPa at a strain rate of 10^{-7} s^{-1}.

The effect of strain rate on the static moduli was low. Although these changes were small, we observed that E_s decreased from 67 GPa in the test performed at a strain rate of 10^{-3} s^{-1} to 65 GPa in the test performed at a strain rate of 10^{-7} s^{-1} and at 75 ºC. K_s only decreased from 1 to 3 GPa with each increment of strain rate increase. The ν_s decreased by 0.01 to 0.02, except in the case of the sample tested at 10^{-5} s^{-1} and at room temperature, it was largest in the test performed at room temperature comparing with the test at elevated temperature for the three different strain rate.

Sample	Strain rate	T	σ_{max}	Max. axial strain	Max. radial strain	E_s	ν_s	K_s
12	10^{-3}	RT	541	0.94	-0.076	69	0.12	24
14	10^{-3}	50	500	0.80	-0.048	68	0.07	26
15	10^{-3}	75	457	0.74	-0.067	67	0.08	23
13	10^{-5}	RT	520	0.91	-0.532	69	0.24	45
11	10^{-5}	50	486	0.88	-0.045	66	0.06	25
17	10^{-5}	75	477	0.85	-0.045	66	0.08	25
10	10^{-7}	RT	486	0.86	-0.055	68	0.11	29
6	10^{-7}	50	481	0.85	-0.045	66	0.06	25
8	10^{-7}	75	429	0.74	-0.041	65	0.06	5

Table 3. Results from the constant temperature triaxial tests at different strain rates. Legend: Strain rate (in s^{-1}); T: temperature at which the test was performed (in °C); σ_{max}: maximum stress (in MPa); Max. axial strain: maximum axial strain reached at the maximum strength (in %); Max. radial strain: maximum radial strain reached at the maximum strength (in %); E_s: static Young's modulus (in GPa); ν_s: static Poisson's ratio; K_s: static bulk modulus (in GPa); confining pressure (P_C) was 25 MPa in all tests; RT: room temperature.

4.3 Cyclic triaxial loading test

Results from the cycling test performed at room temperature, under 25 MPa of confining pressure and a strain rate of 10^{-5} s^{-1} are indicated in Table 4. E_s increased with incremental increases in the applied load stress, but there were no notable changes between cycles at the same stress. The ν_s increased by 0.06 from 0.23 at 60% of peak stress to 0.29 at 80% of peak stress but remained constant when repeatedly loaded at the same stress. K_s increased with the amount of load applied between 5 and 10 GPa but again remained consistent when cycled at the same stress. When the sample was loaded to 80% of the peak stress and the unloading was only to 60% of the peak stress rather than to zero, the E_s was found to be 10 MPa higher than the first cycle at 80 % of the peak stress when the unloading was to zero MPa. Over the same period K_s increased by 8 GPa, but ν_s remained constant.

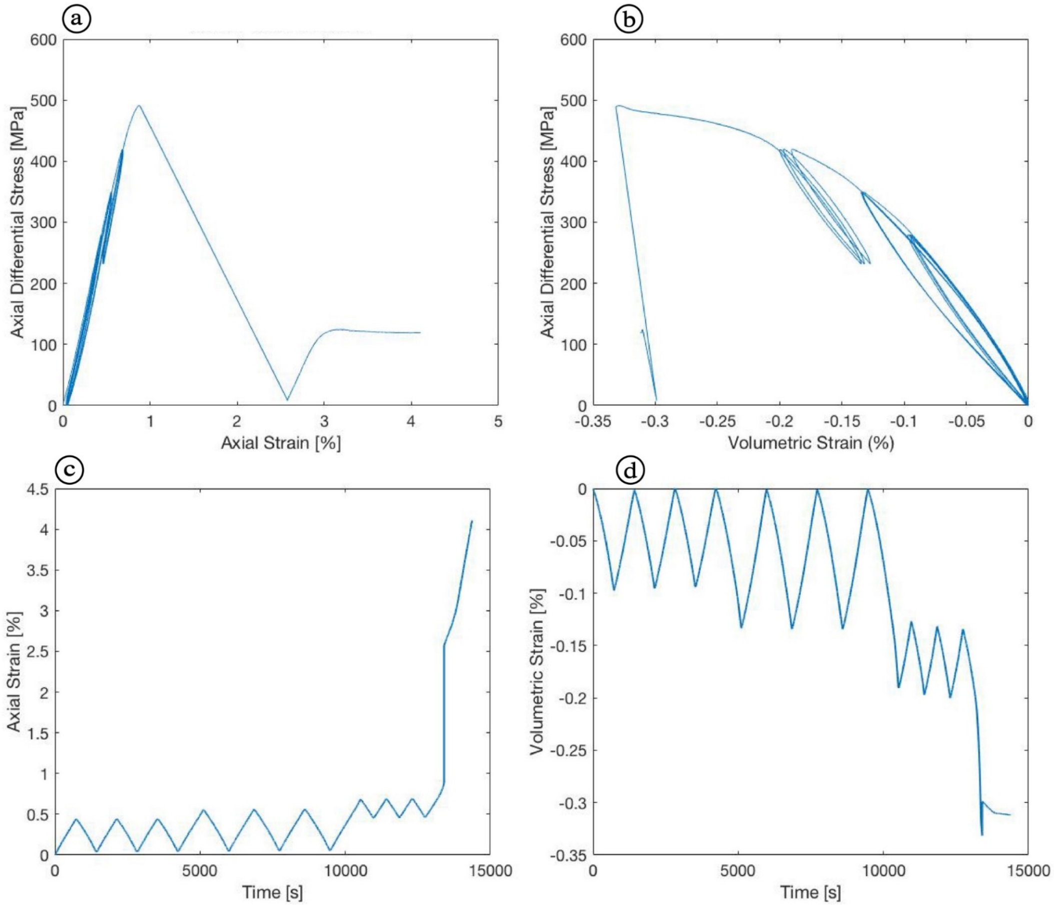

Figure 7. Stress vs strain in a cyclic loading test under confining pressure of 25 MPa and performed at room temperature. a) and b) corresponding axial differential stress against axial strain and volumetric strain, respectively. c) and d) represent axial and radial strain vs time.

Cycle	σ_{load}	E_s	ν_s	K_s
1 at 60%	280	65	0.22	38
2 at 60%	281	68	0.23	41
3 at 60%	280	68	0.23	42
4 at 70%	351	68	0.26	46
5 at 70%	351	68	0.26	46
6 at 70%	351	68	0.26	46
7 at 80%	421	68	0.29	52
8 at 80%	421	77	0.29	60

9 at 80%	421	77	0.29	59

Table 4. Results from a cyclic triaxial loading test at a Pc of 25 MPa and with a strain rate of 10^{-5} s^{-1}. Cycle: the number of the cycle and the percentage of stress prior to failure; σ_{load}: the stress of load for each cycle (in MPa); E_s: static Young's modulus (in GPa); v_s: static Poisson's ratio; K_s: static bulk modulus (in GPa).

4.4 Hydrostatic permeability

The as received samples were measured in a hydrostatic permeameter in order to measure sample permeability, using the steady-state flow method, at different levels of confining pressure. The permeability ranged from 12.2 x 10^{-19} m^2 to 1.01 x 10^{-19} m^2 over the confining pressures tested and generally decreased with increased confining pressure (Table 5). The range of permeabilities measured for each sample was much less at higher confining pressures. We did not measure the permeability of the heat-treated samples.

Pc \ Sample	k m^2 *10^{-19}		
	10 MPa	15 MPa	25 MPa
B1	5.46	3.67	1.92
B3	12.2	7.86	5.71
B4	2.21	6.73	1.01
mean	6.62	6.09	2.88
St. D.	5.10	2.17	2.49

Table 5. Permeability (k, in m^2 x10^{-19}) at different levels of confining pressure (Pc, in MPa). St. D is the standard deviation.

4.5 Microtexture and permeability calculated by μ-CT

The mineralogy of the samples detected through μ-CT scanning is segmented in black in Figure 8. The matrix is predominantly composed by quartz, plagioclase and k-feldspar. Together, these minerals account for ~86.9% of the total minerals. Biotite, chlorite and epidote account for ~12.7% and other dense minerals, compose 0.4% of the total. These percentages are very similar to the values estimated by optical microscopy.

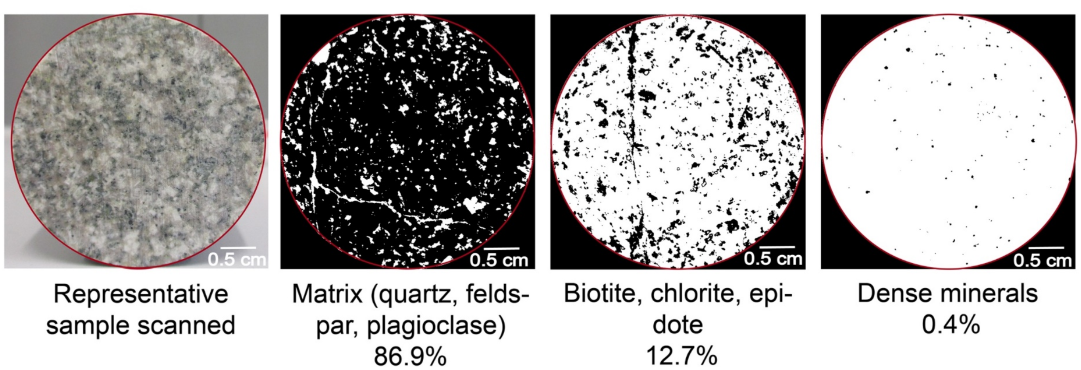

Figure 8. Mineralogy of the scanned sample segmented based on the composition of represented granodiorite sample, where each mineralogy is shown in black.

The samples were scanned after the triaxial deformation and the resulting images display fractures with a range of different orientations, apertures and distributions. Figure 9 shows that most of the samples contained more than one macrofracture, and, in some cases, the fractures were joined at a point and hence generated a connected network. Horizontal macro fractures traversed the center of the sample cores in the three samples loaded without cycling (Fig. 9 a, b, c). On the contrary the sample exposed to cyclic loading (Fig. 9d) exhibited macro fractures that formed obliquely to the two main fractures.

In Figure 10, a 3D visualization of the fractured samples is showed. The colors in these plots relate to the diameter of the aperture in each voxel (three-dimensional pixel). Fractures in the sample tested at a strain rate 10^{-3} s^{-1} and room temperature (Fig. 10 a) were arranged in a more complex way than fractures formed at the other rates. This is because two secondary fractures joined to the main fracture and at this scale the horizontal fractures were not observable in the orthogonal views. As such the range of apertures were between 0 to 9.4×10^{-3} mm^3, and hence larger than the other samples. The sample tested at 10^{-3} s^{-1} and 75 ºC (Fig. 10b), also exhibited a main fracture that joined to a secondary horizontal fracture and the aperture of the main fracture was between 0 to 1.3×10^{-2} mm^3. The sample at 10^{-7} s^{-1} and at room temperature (Fig. 10c) had a main fracture joined to two secondary horizontal fractures where the apertures ranged between 0 and 1.1×10^{-2} mm^3. The sample that was cyclically deformed (Fig. 10d) also exhibited a complex network of fractures, but the aperture of the fractures was smaller than in the other samples ranged between 0 to 4.3×10^{-3} mm^3. In this case, one main fracture joined to a secondary fracture at the end of the core and multiple smaller fractures joined to them forming a network.

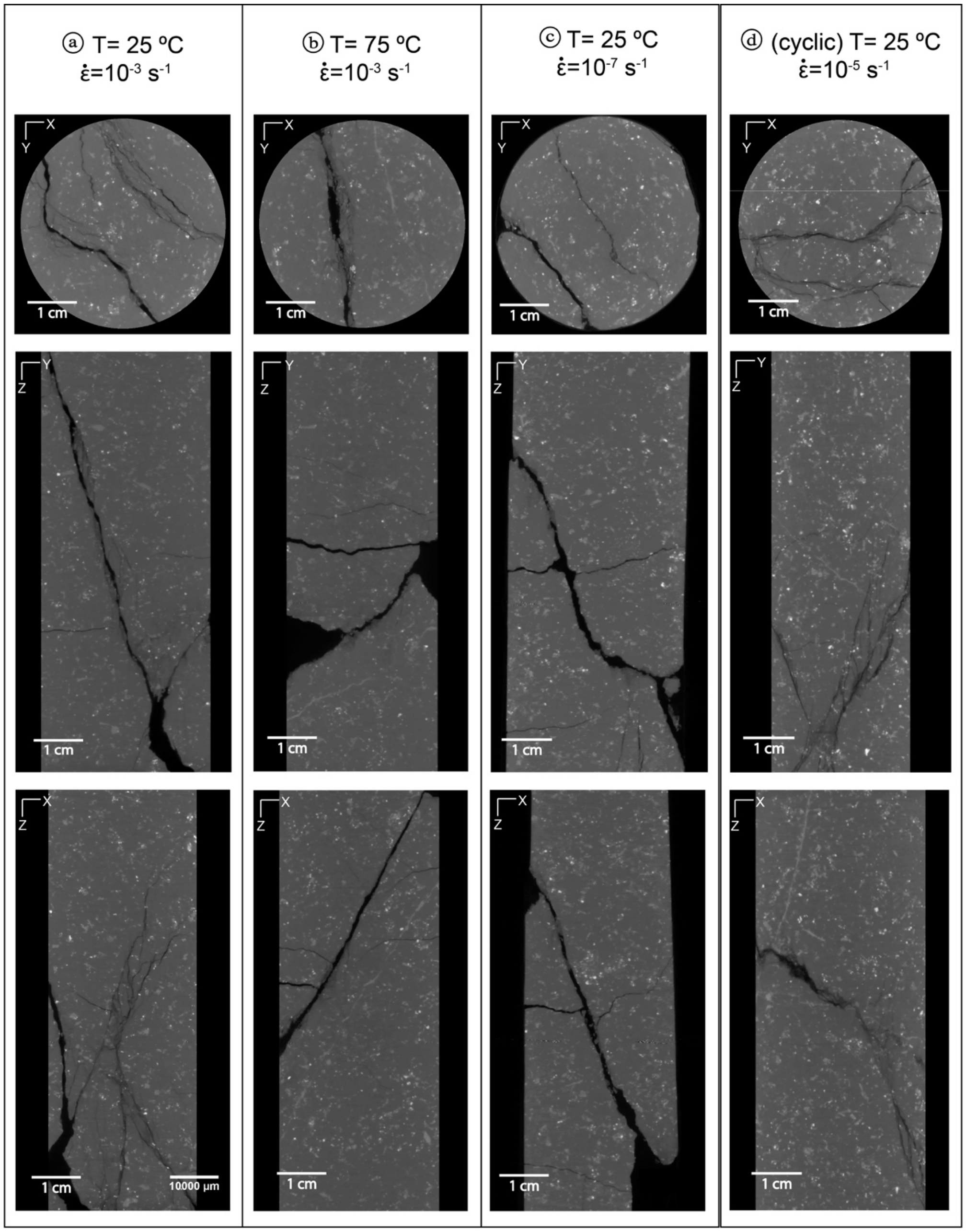

Figure 9. Images of the fractures formed after failure of samples deformed at different strain rates and temperatures. The cross section was taken in the middle of each sample. The three views are orthogonal between them. a) with a strain rate of 10^{-3} s^{-1} and room temperature, b) with a strain rate of 10^{-3} s^{-1} at 75 ºC, c) with a strain rate of 10^{-7} s^{-1} and room temperature, d) a cyclic triaxial test with a strain rate of 10^{-5} s^{-1} and room temperature. All samples deformed with an applied confining pressure of 25 MPa.

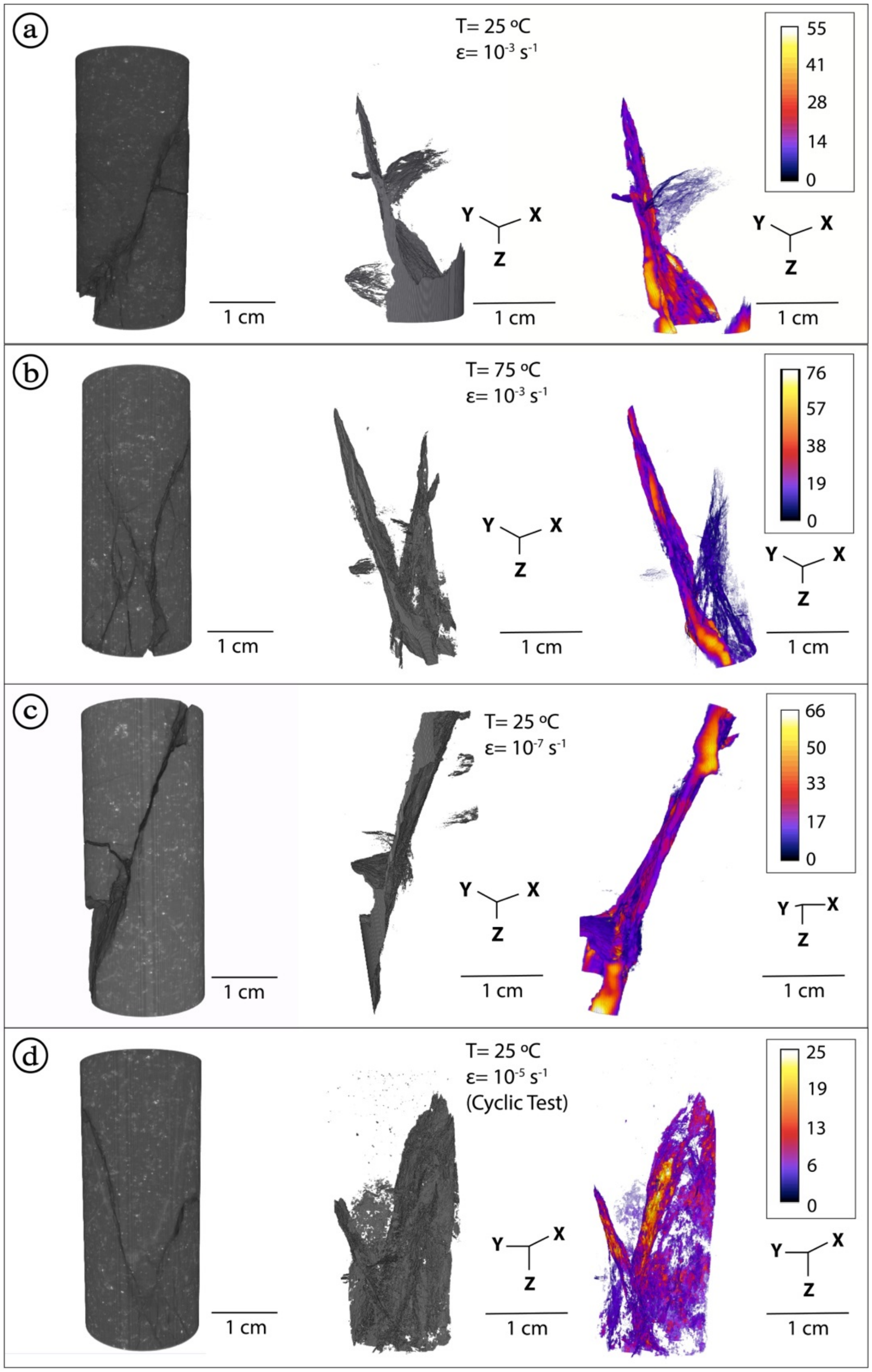

Figure 10. 3D visualization of fracture apertures after sample deformation and failure at different levels of confining pressure and temperature. Each figure represents the 3D reconstruction of the tested sample, the segmented fracture and the aperture measured in voxel and each individual voxel is 1.7×10^{-4} mm^3.

From the segmented fractures we measured the porosity respect to the total volume and permeability was calculated by means of the Lattice Boltzmann method (LBM) and the results are summarized in Table 6. The values of the porosity and permeability show a certain trend between the highest values of both parameters, and vice versa. The porosity varied between 7.92% to 3.93% and the lowest value was the case of the sample in the cycling test and the highest value was for the sample tested at elevated temperature. Additionally, the permeability increased considerably in samples with macro fractures in comparison to the as received samples and varies between 4.86×10^{-10} m^2 to 2.58×10^{-9} m^2 due to the increase in porosity.

Sample	Porosity average (%)	Permeability (m^2)	Velocity Norm
10 (10^{-3} s^{-1}, room temperature)	5.234	2.58×10^{-9}	3.42×10^{-2}
12 (10^{-3} s^{-1}, 75 ºC)	7.921	1.06 E$\times10^{-9}$	1.40×10^{-2}
15 (10^{-7} s^{-1}, room temperature)	4.239	8.23×10^{-10}	1.09×10^{-2}
2 (10^{-5} s^{-1}, room temperature, cycling test)	3.931	4.86×10^{-10}	6.44×10^{-3}

Table 6. Calculated permeability (in m^2) of each sample derived from the image scans using the Lattice Boltzmann Method.

The fractures are also visualized in Figure 11, where it is possible to observe the fluid velocity through the sample. In all four cases, the fluid velocity was fastest in the main fracture and slowest in the secondaries/subordinated fractures. The permeability also changed spatially through the fractures where in most cases the velocity was fastest at the top of the sample volume and slowest at the bottom, except in the sample tested in the cyclic test where the velocity was largest in the middle of the fracture. The velocity average varied between 3.42×10^{-2} to 6.44×10^{-3}, the lower values measured were obtained in the sample which was cyclically loaded, and the higher values were for the samples tested at 10^{-3} s^{-1} and at room temperature.

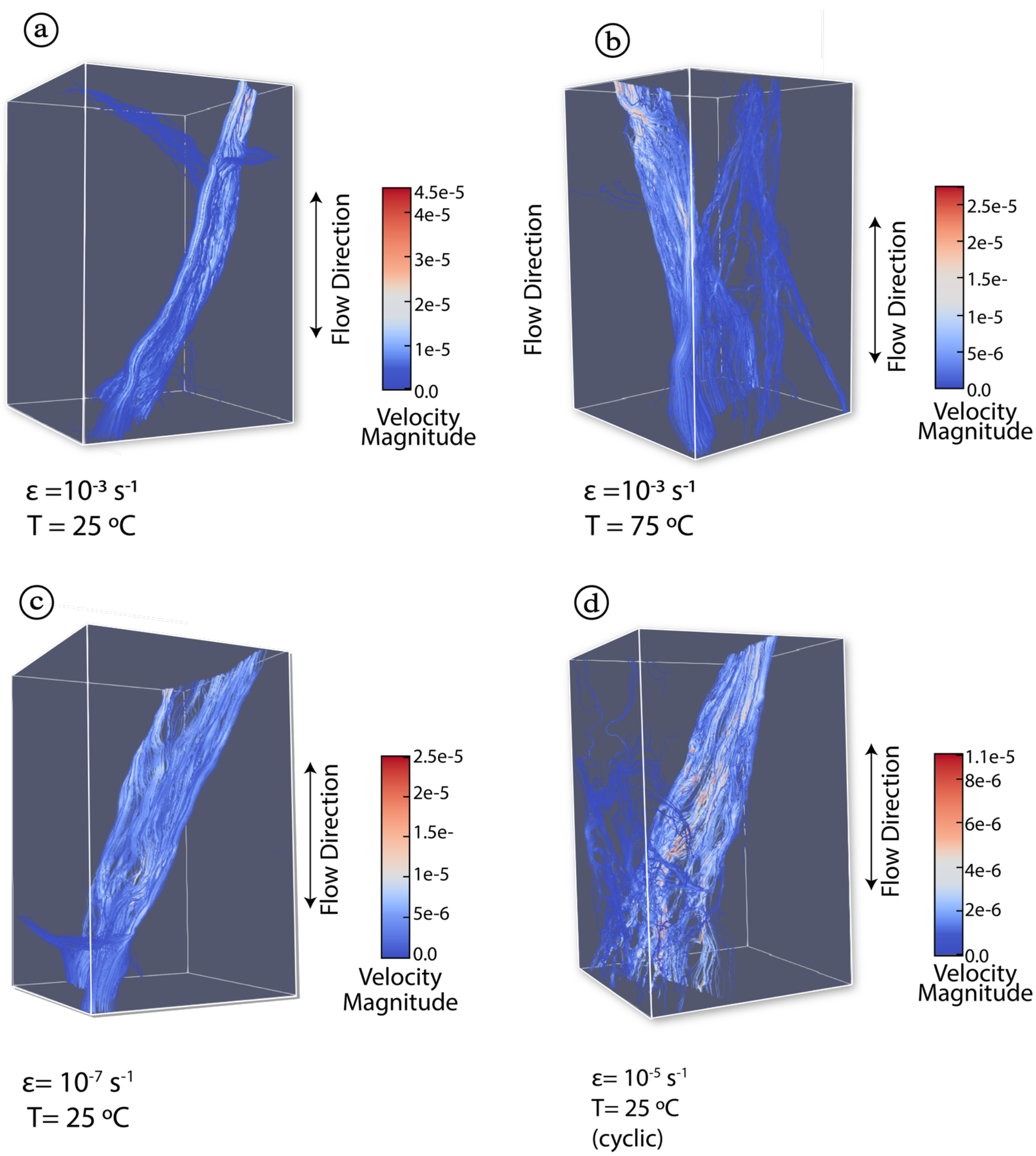

Figure 11. 3D visualization of fluid velocities through the imaged fractures. a) sample deformed with a strain rate of 10^{-3} s^{-1} at room temperature, b) deformed with a strain rate of 10^{-3} s^{-1} but at 75°C, c) deformed with a strain rate of 10^{-7} s^{-1} at room temperature, d) cyclic triaxial deformation with a strain rate of 10^{-5} s^{-1} at room temperature. All tests were performed at a confining pressure of 25 MPa.

5 DISCUSSION

5.1 Thermo-mechanical properties of granodiorite

The results presented here have highlighted the influence of thermal treatment on changing the physical properties and deformation behavior of a geothermal reservoir analogue rock, namely the Liquiñe granodiorite. These changes were observed through measurements of ultrasonic velocity waves, capillarity and mechanical deformation.

Microfractures induced following heat treatment were also observed under the electronic microscope and commonly formed as intergranular cracks around quartz, plagioclase and feldspar crystals. The formation of these cracks is, at least, partly due to the different influence of temperature on the thermal expansion of each mineral type in the rock. For example, the proportion of quartz is an important factor in the generation of thermal cracks because this mineral type has relatively high thermal expansion coefficient (Siegesmund et al., 2018; Vazquez et al., 2018) (38×10^{-6} K^{-1}) when compared with other minerals, such as feldspars (8.7×10^{-6} K^{-1}) (Fei, 1995; Huotari & Kukkonen, 2004). As such, it is the difference in thermal expansion or thermal expansion anisotropy between minerals or within individual minerals that greatly contributes to the formation of thermal cracks. In this regard, Meredith et al. (2001) noted a significant thermal expansion anisotropy within individual quartz minerals which develops an internal strain deficit leading to thermal cracking. Quartz, feldspar and plagioclase represent more than 86% of the total composition of this granodiorite and are therefore the key minerals with respect to the formation of the thermal cracks, so it is not unexpected that the microcracks formed around to these minerals.

The influence of the developed thermal cracks can be recorded through increases in capillarity with increasing levels of temperature treatment. This observation suggests that the nucleation and growth of these micro-fractures can create an efficient mechanism for generating interconnected networks that make pathways for fluids. The interpretation of thermally induced cracking is further supported by decreases in both V_P and V_S parameters with increasing temperature treatment to the maximum temperature tested at 210 ºC. Similar ultrasonic wave measurement observations have been described by Zhu et al., (2017) who noted a decrease in V_P even when their granite was heated to only 100 ºC.

However, they noted larger changes when the samples were heated more than 400 ºC, which they, and other authors, have attributed to mineral dehydration and the passing of the quartz alpha/beta transition (Chaki et al, 2008; Chen et al., 2014, Shao et al., 2015). As such, the combined observation by means of electronic microscope, capillarity variation and the change in the ultrasonic wave velocities support the notion that temperature treatment induced thermal damage in the samples. However, the porosity data appears to contradict the other evidence as porosities are shown to decreasing with increments of temperature. We attribute the changes in porosity to natural sample variability and hence whilst there is an apparent decrease the range of change is within the standard deviation of measurements. This suggests that porosity is not the best indicator to determine changes in the amount of thermal cracking.

About the mechanical data, both strength and stiffness tended to decrease in samples heated to higher temperatures. In the mechanical tests performed at both ambient and confined pressure we found a significant reduction in the elastic moduli in those samples heated to 210 ºC but the samples heated to 150ºC had similar properties to the as-received samples. Reductions in strength and elastic moduli with temperature treatment have been previously observed when the samples were deformed at elevated temperatures between 300 ºC and 100 ºC (Zhu et al., 2017). In our mechanical tests performed in the thermo-triaxial equipment, the temperatures were below 100 ºC. We found that temperature has the effect of decreasing the peak stress by almost 40 MPa from the room temperature tests. In fact, the changes in strength were most notable when comparing the test performed at room temperature and at 50 ºC. There was comparatively little change in strength when comparing the sample strength deformed at 50 ºC to that at 75 ºC. The influence of elevated temperature cannot be attributed to the formation of thermal cracks because all of the tests were performed at temperatures lower than the threshold for thermal damage (i.e < 150 ºC). However, it has been suggested that the pre-existing fractures control the cracking of the rock longer than fractures induced by thermal stress (Wang et al., 2013). As such, a different mechanism is needed to explain the strength reduction with temperature. It has been suggested that the amount of sub-critical cracking increases with temperature and hence favored to reduce the strength of rocks at elevated temperatures (Tullis & Yund, 1977; Kranz et al., 1982; Heap et al., 2009).

Our results support previous studies which indicate that the mechanical behavior of rocks is influenced by strain rate, where both rock strength and stiffness increase at higher strain rates (Fig. 12) (Kumar, 1968; Blanton, 1981; Lajtau et al., 1991). This observation has a two-fold explanation; firstly, incremental increases in strain rate produce incremental increases in the stress factor intensity (K_{IC}) which encourages sub-critical crack growth (Meredith et al., 1985). Secondly, at lower strain rates there is more time available for the development of sub-critical crack growth and so samples have lower strengths.

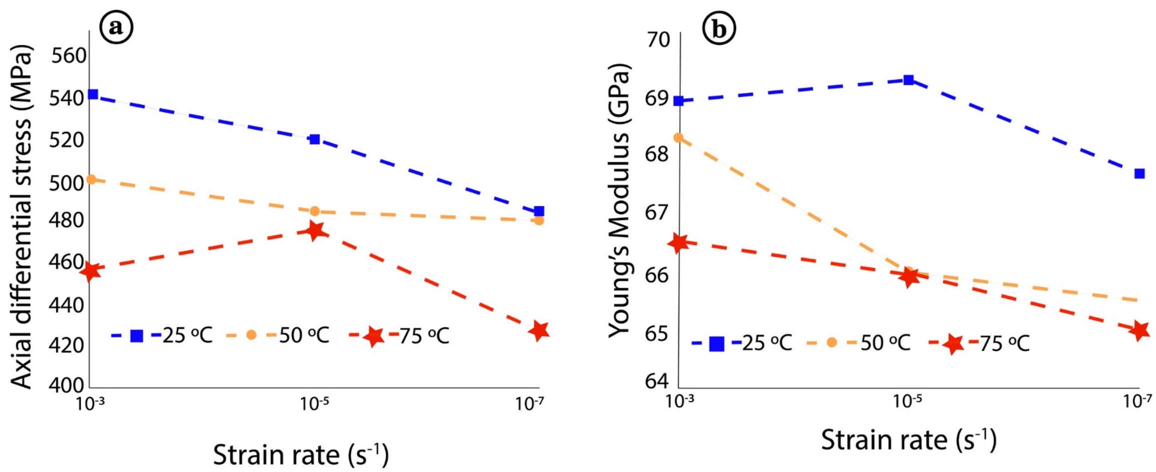

Fig. 12 a) Max. axial differential stress and b) static Young's modulus as a function of strain rate during conventional thermo-triaxial deformation experiments on as-received samples at confining pressures of 25 MPa and indicated temperatures of 25, 50, and 75 °C.

In our cyclic mechanical loading tests, we observed several stages of deformation. Loading up to 13% of the rock strength produced sample shortening through decreases in the axial strain which is indicative of the closure of fractures aligned normal to the applied axial differential stress. Between 13% and 70% of the rock strength the deformation behavior was elastic as confirmed by repeated cycling within this range. We note that the strain and stress display the same pattern in each cycle regardless of the number cycles that were performed. Above 70 % of the rock strength we noted significant increases in the radial strain, which is indicative of fracture dilation, and we do note a small increase of between 1-3 GPa in the Young's modulus between the range of loading between 60% and 70% of the peak stress. This is as expected as new fracture damage would not be created until a higher level of stress is reached, assuming the rock possesses a Kaiser 'damage memory' effect (Lockner, 1993; Browning et al., 2017; Browning et al., 2018). Our findings are similar to those results from other granitic rocks which suggest that cyclic loading to higher levels of stress produces a reduction in both the elastic moduli and strength (Heap & Faulkner, 2008). This occurs because of an increase in the level of damage with increasing stress in each cycle (Kranz et al., 1982; Heap et al., 2009). For example, in Westerly Granite the results obtained by Mitchell & Faulkner (2008) indicated deformation up to 80% of the peak stress was inelastic.

Results from the Lattice Boltzmann models show that most samples, except in the cyclic test, exhibit a main axially aligned fracture, at approximately 45° to the loading direction, which is connected to a set of near horizontally aligned secondary fractures. It is the connection between the two sets of fractures that generate a greater level of interconnectivity and hence permeability. It is no clear if the secondary fracture set was formed during sample unloading, however the rate of unloading was slow to avoid a catastrophic rupture. The resolution of 55.43 μm limits the apertures of measured and modelled micro-fractures. Those fractures with apertures smaller than resolution were not considered in the calculation of permeability. It is known that both micro-fractures and macro-fractures contribute to the permeability (i.e. Bonnet et al., 2001; Bour et al., 2002), however permeability is predominantly controlled by macro fractures when they are present and in this case, the contribution of microfractures is less (Davy et al., 2006; Nara et al., 2011). In short timescales permeability is controlled by macrofractures but over longer timescales microfractures have a greater influence on permeability (Bonnet et al, 2001). Our results show that fluids flow more easily through the main fractures than the secondary fractures, and therefore they control the permeability of the tested samples. This can be explained because the apertures of the main fractures are larger than the secondary fractures and the main fractures are orientated more favorably to the fluid direction than the other fractures.

5.2 Application to the Liquiñe geothermal reservoir

The applied confining pressure can be considered as equivalent to the lithostatic pressure, where 10 MPa represents ~ 0.5 km in depth and 25 MPa represents ~1 km of depth. At these pressures and depths fractures and porosity can become closed and hence substantially impact in the permeability, stiffness and strength of the rock. In this case it would be expected that a greater level of differential stress would be required to fracture the rock and generate new fluid paths or maintain the initial fluid paths with depth. It has been shown however, that it is possible for fractures to remain partially open at confining pressures highest than 100 MPa when a significantly high pore pressure is applied (Violay et al., 2017). This indicates that permeability, at depth in a geothermal reservoir, depends on the pore fluid pressure inside the rocks. If a pore fluid pressure is applied to generate new fractures or extend pre-existing fractures, then the permeability will increase similarly to as was reported by the results of our Lattice Boltzmann model. Pérez-Flores et al. (2017) measured the change in permeability with increasing effective pressure in five rock types near the Lonquimay area, Chile (~38º S), one of which was a granodiorite. They concluded that the granodiorite permeability was around 10^{-19} m^2, similar to that obtained here, but the permeability also increased by orders of magnitude when a macro-fracture was formed.

For the Liquiñe granodiorite, which is a potential reservoir hosting rock of the Liquiñe geothermal system, the input of thermal cracking damage was reported at temperatures between 150 ºC to 210 ºC which was an important, but not the main factor in the reduction of strength and elastic moduli. The geothermal gradient is poorly constrained in the Liquiñe region but in other parts of Chile ranges from between ~25 ºC/km up to ~75 ºC/km (Muñoz and Hamza, 1993). This would indicate that mechanisms of thermal damage would influence the strength and stiffness of reservoir rocks at depths of between around 2 to 6 km. At the depth estimated for the reservoir of Liquiñe, ~3 km (Held et al., 2018) rocks would hence not be affected by thermal cracking damage as due to the geothermal gradient but still may be locally affected by interaction of hot fluids passing through a permeable fracture network. The Liquiñe region is characterized by hot fluids circulating in a fracture network at temperatures between 80 ºC and 150 ºC (Sánchez et al., 2013; Held et al., 2018). The higher end of these fluid circulating temperatures would be sufficient to generate thermal cracking damage around the permeable network of fractures which over time would lead to the development of new fractures, fracture network connectivity and increased permeability.

The Liquiñe region is also characterized by a distribution of crustal faults which likely impose a control on the distribution of fracture damage and hence crustal permeability (Pérez-Flores et al., 2016). At depths below around 1 km, macrofractures would likely become closed and hence fluids would only be able to access microfractures unless there is a sufficiently high pore fluid pressure (i.e. Violay et al., 2017). Our findings suggest that the granodiorite from Liquiñe is with a very low intrinsic permeability (of < 10^{-19} m^2). So, it is likely that the vast majority of fluids must be transported through or near faults where the permeability is expected to be greatest. Results from our imaging and modelling indicate that open fractures aligned parallel to any vertical fluid flow would store hot fluids rather than substantially contribute to their mobility (Sánchez et al., 2013; Pérez-Flores et al., 2016; Roquer et al., 2017).

6 CONCLUSIONS

We reported on the physical properties of a Liquiñe granodiorite which represents a natural geothermal reservoir hosting analogue rock. In order to discern changes in the physical rock properties and mechanical behavior in the rock at reservoir conditions, we heated the rocks to realistic reservoir temperatures to induce thermal crack damage. We found that the granodiorite does thermally crack at temperatures > 150 ºC and the effect of the thermal crack damage is to reduce both the strength and the stiffness of the rock. In the Liquiñe reservoir such temperatures and hence physical rock property changes could be expected between around 2 to 6 km depth. At shallower depths, for example the depth estimated for the reservoir (~3 km) thermal cracking will form only at the margin of fractures when sufficiently hot fluids pass through the fractures. The implication is that this process could potentially extend the fracture network and hence increase the rock permeability which is intrinsically very low (< 10^{-19} m^2).

We also performed a suite of mechanical deformation tests at elevated temperature and pressure conditions and under different strain rates. The results indicate that the rock strength can decrease with only small increments of higher temperature (room temperature, for example in our tests), and then deformed more slowly. These observations cannot be explained through the development of thermal crack damage as the temperatures were too low. However, the results are complementary and can instead be explained through the development of sub-critical cracking which is favored during slow deformation, where there is more time available for sub-critical crack growth, and at elevated temperature where there is a greater level of activation energy for sub-critical crack growth. The onset of fracture damage in our cyclic loading test at room temperature was found to occur at around 80% of the peak stress (or failure stress).

In the context of the Liquiñe geothermal reservoir it is likely that the highest permeabilities are concentrated in and around the main fault zones, over short timescales, and these permeability concentrations are represented by the location of hot springs on the main fault strands of the LOFS and ATF. However, over longer timescales, > 500 years, processes of thermal cracking and sub-critical crack growth can conspire to produce a highly fractured reservoir atop a heat source but likely required the fault zone for its initiation.

ACKNOWLEDGMENTS

This research was financed by project FONDECYT n°1180167 project, and it was a contribution with FONDAP n°15090013 project "*Centro de Excelencia en Geotermia de los Andes*" (CEGA). The FONDEQUIP Nº EQM150101 project provided the FE-SEM equipment. We thank to Editors and anonymous Reviewers for their comments and suggestions, which enhanced the manuscript. We also thank Kristian Kroll and Martin Balcewicz for their support in the Laboratories of Geotechnologies and Seismic Observation at the GZB. Authors thank Guillermo Poblete for his help in mechanical and petrophysical experiments, and Rodrigo Gomila for his insights on the permeability modelling. We thank to Domingo Mery for his comments on images segmentation, and Ferdinand Stöckhert for his assistance in the permeability test in the Engineering Geology Laboratory at the RUB. Tomás Roquer acknowledges support from CONICYT doctoral grant nº21171178.

REFERENCES

Ahrens, J., Geveci, B., & Law, C. (2005). ParaView: An End-User Tool for Large-Data Visualization, Visualization Handbook, Elsevier, ISBN-13 978-0123875822

Andrä, H., Combaret, N., Dvorkin, J., Glatt, E., Han, J., Kabel, M., Keehm, Y., Krzikalla, F., Lee, M., Madonna, C., Marsh, M., Mukerji, T., Saenger, E. H., Sain, R., Saxena, N., Ricker, S., Wiegmann, A., & Zhan, X. (2013). Digital rock physics benchmarks -Part I: Imaging and segmentation. *Computers and Geosciences*, *50*, 25–32. https://doi.org/10.1016/j.cageo.2012.09.005

Angermann, D., Klotz, J., & Reigber, C., (1999). Space-geodetic estimation of the Nazca-south America euler vector. Earth and Planetary Science Letters, 171, 329-334.

Anissofira, A., & Latief, F. D. E. (2015). Permeability Estimation of Crack Type and Granular Type of Pore Space in a Geothermal Reservoir Using Lattice Boltzmann Method and Kozeny-Carman Relation. *World Geothermal Congress 2015*, 8.

Arancibia, Cembrano, L, & Lavenu, A., (1999). Transgresión dextral y partición de deformación en ZFLO. *Revista Geologica de Chile*, *26*, 3-22. Retrieved from http://dx.doi.org/10.4067/S0716-02081999000100001.

Aravena, D., Muñoz, M., Morata, D., Lahsen, A., Parada, M. Á., & Dobson, P. (2016). Assessment of high enthalpy geothermal resources and promising areas of Chile. *Geothermics*, *59*, 1–13. https://doi.org/10.1016/j.geothermics.2015.09.001

ASTM, *D7012-10*, (C). (2010). Standard test method for compressive strength and elastic moduli of intact rock core specimens under varying states of stress and temperatures., 1–8. https://doi.org/10.1520/D7012-13.1

ASTM, D2485. (2005). Standard Test Method for Laboratory Determination of Pulse Velocities and Ultrasonic Elastic Constants of Rock, 5–11. https://doi.org/10.1520/D2845-08.2

Atkinson, B. K. (1984). Subcritical crack growth in geological materials. *Journal of Geophysical Research: Solid Earth*, *89*(B6), 4077-4114

Bauer, J. F., Krumbholz, M., Meier, S., & Tanner, D.C. (2017). Predictability of properties of a fractured geothermal reservoir: the opportunities and limitations of an outcrop analogue study. Geothermal Energy, 5(1), 24.

Blanton, T. L. (1981). Effect of strain rates from 10^{-2} to 10 sec^{-1} in triaxial compression tests on three rocks. *International Journal of Rock Mechanics and Mining Sciences & Geomechanical Abstracts*, *18* (1), 47–62. https://doi.org/10.1016/0148-9062(81)90265-5

Bonnet, E., Bour, O., Odling, N. E., Davy, P., Main, I., Cowie, P., & Berkowitz, B.: Scaling of fracture systems in geological media. *Reviews of Geophysics*, **39** (2001), 347–383.

Bour, O., Davy, P., Darcel, C., Ödling, N.: A statistical scaling model for fracture network geometry, with validation on multiscale mapping of a joint network (Hornelen Basin, Norway), *Journal of Geophysics Research*, **107** (2002).

Brace, W. F., & Byerlee, J. D. (1966). Stick-Slip as a Mechanism for Earthquakes Author (s): W. F. Brace and J. D. Byerlee. *Science*, *153*(3739), 990–992.

Brantut, N., Heap, M. J., Meredith, P. G., & Baud, P. (2013). Time-dependent cracking and brittle creep in crustal rocks: A review. *Journal of Structural Geology*, *52*, 17-43

Browning, J., Meredith, P., & Gudmundsson, A. (2016). Cooling-dominated cracking in thermally stressed volcanic rocks. *Geophysical Research Letters*, *43*(16), 8417–8425. https://doi.org/10.1002/2016GL070532

Browning, J., Meredith, P. G., Stuart, C. E., Healy, D., Harland, S., & Mitchell, T. M. (2017). Acoustic characterization of crack damage evolution in sandstone deformed under conventional and true triaxial loading. *Journal of Geophysical Research: Solid Earth*, *122*(6), 4395–4412. https://doi.org/10.1002/2016JB013646

Browning, J., Meredith, P. G., Stuart, C., Harland, S., Healy, D., & Mitchell, T. M. (2018). A Directional Crack Damage Memory Effect in Sandstone Under True Triaxial Loading. *Geophysical Research Letters*, 45, 6878-6886. https://doi.org/10.1029/2018GL078207

Bultreys, T., De Boever, W., & Cnudde, V. (2016). Imaging and image-based fluid transport modeling at the pore scale in geological materials: A practical introduction to the current state-of-the-art. *Earth-Science Reviews*, *155*, 93–128. https://doi.org/10.1016/j.earscirev.2016.02.001

Castagna, A., Ougier-Simonin, A., Benson, P. M., Browning, J., Walker, R. J., Fazio, M., & Vinciguerra, S. (2018). Thermal Damage and Pore Pressure Effects of the Brittle-Ductile Transition in Comiso Limestone. *Journal of Geophysical Research: Solid Earth, 123, 7644-7660*. https://doi.org/10.1029/2017JB015105

Cembrano, J., & Herve, F. (1993). The Liquiñe Ofqui Fault Zone: a major Cenozoic strike slip duplex in the Southern Andes. *Second ISAG*, 175–178.

Cembrano, J., Hervé, F., & Lavenu, A. (1996). The Liquiñe Ofqui fault zone: a long-lived intra-arc fault system in southern Chile. *Tectonophysics*, *259*(1–3), 55–66. https://doi.org/10.1016/0040-1951(95)00066-6

Cembrano, J., & Lara, L. (2009). The link between volcanism and tectonics in the southern volcanic zone of the Chilean Andes: A review. *Tectonophysics*, *471*(1–2), 96–113. https://doi.org/10.1016/j.tecto.2009.02.038

Chaki, S., Takarli, M., & Agbodjan, W. P. (2008). Influence of thermal damage on physical properties of a granite rock: Porosity, permeability and ultrasonic wave evolutions. *Construction and Building Materials*, *22*(7), 1456–1461. https://doi.org/10.1016/j.conbuildmat.2007.04.002

Chen, L., Liu, J. F., Wang, C. P., Liu, J., Su, R., & Wang, J. (2014). Characterization of damage evolution in granite under compressive stress condition and its effect on permeability. *International Journal of Rock Mechanics & Mining Sciences, 71*, 340–349. https://doi.org/10.1016/j.ijrmms.2014.07.020

Chen, S., Yang, C., & Wang, G. (2017). Evolution of thermal damage and permeability of Beishan granite. *Applied Thermal Engineering*, *110*, 1533–1542. https://doi.org/10.1016/j.applthermaleng.2016.09.075

Cho, W. J., Kwon, S., & Choi, J. W. (2009). The thermal conductivity for granite with various water contents. *Engineering Geology*, *107*(3–4), 167–171. https://doi.org/10.1016/j.enggeo.2009.05.012

Cnudde, V., & Boone, M. N. (2013). High-resolution X-ray computed tomography in geosciences: A review of the current technology and applications. *Earth Science Reviews*, *123*, 1–17. https://doi.org/10.1016/j.earscirev.2013.04.003

David, C., Menéndez, B., & Darot, M. (1999). Influence of stress-induced and thermal cracking on physical properties and microstructure of La Peyratte granite. *International Journal of Rock Mechanics and Mining Sciences*, *36*(4), 433–448. https://doi.org/10.1016/S0148-9062(99)00010-8

Davy, P., Bour, O., de Dreuzy, J.-R., Darcel, C.: Flow in multiscale fractal fracture networks. *Fractal Analysis for Natural Hazards,* **261** (2006), 31–45.

Doube, M., Klosowski, M. M., Arganda-Carreras, I., Cordelières, F. P., Dougherty, R. P., Jackson, J. S., Schmidt, B., Hutchinson, J. R., & Shefelbine, S. J. (2010). BoneJ: Free and extensible bone image analysis in ImageJ. *Bone*, *47*(6), 1076–1079. https://doi.org/10.1016/j.bone.2010.08.023

Duda, M., & Renner, J. (2013). The weakening effect of water on the brittle failure strength of sandstone. *Geophysical Journal International*, *192*(3), 1091–1108. https://doi.org/10.1093/gji/ggs090

Dwivedi, R. D., Goel, R. K., Prasad, V. V. R., & Sinha, A. (2008). Thermo-mechanical properties of Indian and other granites. *International Journal of Rock Mechanics and Mining Sciences*, *45*(3), 303–315. https://doi.org/10.1016/j.ijrmms.2007.05.008

Faulkner, D. R., Jackson, C. A. L., Lunn, R. J., Schlische, R. W., Shipton, Z. K., Wibberley, C. A. J., & Withjack, M. O. (2010). A review of recent developments concerning the structure, mechanics and fluid flow properties of fault zones. *Journal of Structural Geology*, *32*(11), 1557–1575. https://doi.org/10.1016/j.jsg.2010.06.009

Fei, Y. (1995) Thermal expansion. In: Ahrens, T.J. (ed.) Mineral physics and crystallography. American Geophysical Union, Washington, DC, pp 29–44

Friedrich, J. T., & Wong, T.-f. (1986) Micromechanics of thermally induced cracking in three crustal rocks. *Journal Geophysics Research,* 91, 12743–12764

Gautam, P. K., Verma, A. K., Jha, M. K., Sharma, P., & Singh, T. N. (2018). Effect of high temperature on physical and mechanical properties of Jalore granite. *Journal of Applied Geophysics*, *159*, 460–474. https://doi.org/10.1016/j.jappgeo.2018.07.018

Géraud, Rosener, M., Surma, F., Place, J., Le Garzic, E., & Diraison, M, Y. (2010). Physical properties of fault zones within a granite body: Example of the Soultz-sous-Fôrets geothermal site. *Comptes Rendus Geoscience*, *707*(7–8), 9–16. https://doi.org/10.1016/j.crte.2010.02.002

Glover, P. W. J., Baud, P., Darot, M., Meredith, P., Boon, S. A., LeRavalec, M., ... & Reuschlé, T. (1995). α/β phase transition in quartz monitored using acoustic emissions. *Geophysical Journal International*, 120(3), 775-782.

Griffiths, L., Lengliné, O., Heap, M. J., Baud, P., & Schmittbuhl, J. (2018). Thermal Cracking in Westerly Granite Monitored Using Direct Wave Velocity, Coda Wave Interferometry, and Acoustic Emissions. *Journal of Geophysical Research: Solid Earth*, *123*(3), 2246–2261. https://doi.org/10.1002/2017JB015191

Guo, H., Guo, W., Zhai, Y., & Su, Y. (2017). Experimental and modeling investigation on the dynamic response of granite after high-temperature treatment under different pressures. *Construction and Building Materials*, *155*, 427–440. https://doi.org/10.1016/j.conbuildmat.2017.08.090

Heap, M. J., Vinciguerra, S., & Meredith, P. G. (2009). The evolution of elastic moduli with increasing crack damage during cyclic stressing of a basalt from Mt. Etna volcano. *Tectonophysics*, *471*(1–2), 153–160. https://doi.org/10.1016/j.tecto.2008.10.004

Heap, M. J., & Faulkner, D. R. (2008). Quantifying the evolution of static elastic properties as crystalline rock approaches failure. *International Journal of Rock Mechanics and Mining Sciences*, 45(4), 564-573.

Held, S., Schill, E., Schneider, J., Nitschke, F., Morata, D., Neumann, T., & Kohl, T. (2018). Geochemical characterization of the geothermal system at Villarrica volcano, Southern Chile; Part 1: Impacts of lithology on the geothermal reservoir. *Geothermics*, *74*, 226–239. https://doi.org/10.1016/j.geothermics.2018.03.004

Hervé, F., Pankhurst, R. J., Drake, R., Beck, M. E., & Mpodozis, C. (1993). Granite generation and rapid unroofing related to strike-slip faulting, Aysén, Chile. *Earth and Planetary Science Letters*, *120*(3–4), 375–386. https://doi.org/10.1016/0012-821X(93)90251-4

Hokka, M., Black, J., Tkalich, D., Fourmeau, M., Kane, A., Hoang, N. H., Li, C. C., Chen, W. W., & Kuokkala, V. T. (2016). Effects of strain rate and confining pressure on the compressive behavior of Kuru granite. *International Journal of Impact Engineering*, *91*, 183–193. https://doi.org/10.1016/j.ijimpeng.2016.01.010

Homand-Etienne, F., & Houpert, R. (1989). Thermally induced microcracking in granites: characterization and analysis. *International Journal of Rock Mechanics and Mining Sciences & Geomechanics Abstracts*, 26(2), 125-134.

Huang, Y. H., Yang, S. Q., Ranjith, P. G., & Zhao, J. (2017). Strength failure behavior and crack evolution mechanism of granite containing pre-existing non-coplanar holes: Experimental study and particle flow modeling. *Computers and Geotechnics*, *88*, 182–198. https://doi.org/10.1016/j.compgeo.2017.03.015

Huotari, T., & Kukkonen, I. (2004) Thermal expansion properties of rocks: literature survey and estimation of thermal expansion coefficient for Olkiluoto mica gneiss. Posiva Oy, Olkiluoto, Working Report, vol 4, p 62.

Kranz, R. L., Harris, W. J., & Carter, N. L. (1982). Static fatigue of granite at 200 C. *Geophysical Research Letters*, 9(1), 1-4.

Kumar, A. (1968). The effect of stress rate and temperature on the strength of basalt and granite. *Geophysics*, *33*(3), 501–510.

Kumari, W. G. P., Ranjith, P. G., Perera, M. S. A., Shao, S., Chen, B. K., Lashin, A., Arifi, N. Al., & Rathnaweera, T. D. (2017). Geothermics Mechanical behaviour of Australian Strathbogie granite under in-situ stress and temperature conditions: An application to geothermal energy extraction. *Geothermics*, *65*, 44–59. https://doi.org/10.1016/j.geothermics.2016.07.002

Lahsen, A., Muñoz, N., & Parada, M. A. (2010). Geothermal Development in Chile. *Proceedings World Geothermal Congress*, 25–29. Retrieved from www.cne.cl

Lajtai, E. Z., Duncan, E. J. S., & Carter, B. J. (1991). The Effect of Strain Rate on Rock Strength, *Rock Mechanics and Rock Engineering*, *24*, 99–109.

Lara, L. & Moreno, H., (2004). Geología del área Liquiñe-Neltume. Regiones de Los Lagos y de La Araucanía. servicio Nacional de Geología y Minería. Carta Geológica de Chile, Serie Geología Básica, No 83, p. 23, 1 mapa 1:100.000

Latief, F. D. E., & Fauzi, U. (2012). Kozeny-Carman and empirical formula for the permeability of computer rock models. *International Journal of Rock Mechanics and Mining Sciences*, *50*, 117–123. https://doi.org/10.1016/j.ijrmms.2011.12.005

Lavrov, A. (2001). Kaiser effect observation in brittle rock cyclically loaded with different loading rates. *Mechanics of Materials*, *33*(11), 669–677. https://doi.org/10.1016/S0167-6636(01)00081-3

Lavrov, A. (2003). The Kaiser effect in rocks: Principles and stress estimation techniques. *International Journal of Rock Mechanics and Mining Sciences*, *40*(2), 151–171. https://doi.org/10.1016/S1365-1609(02)00138-7

Liang, C., Wu, S., Li, X., & Xin, P. (2015). Effects of strain rate on fracture characteristics and mesoscopic failure mechanisms of granite. *International Journal of Rock Mechanics and Mining Sciences*, *76*, 146–154. https://doi.org/10.1016/j.ijrmms.2015.03.010

Lockner, D. A. (1993). The Role of Acoustic Emission in the Study of Rock Fracture. *International Journal of Rock Mechanics Mining Sciences and Geomechanics Mining Sciences and Geomechanics*, *30*, 883–899.

Meredith, P. G., Knight, K. S., Boon, S. A., & Wood, I. G. (2001). The microscopic origin of thermal cracking in rocks: An investigation by simultaneous time-of-flight neutron diffraction and acoustic emission monitoring. *Geophysical Research Letters*, *28*(10), 2105–2108. https://doi.org/10.1029/2000GL012470

Mitchell, T. M., & Faulkner, D. R. (2008). Experimental measurements of permeability evolution during triaxial compression of initially intact crystalline rocks and implications for fluid flow in fault zones. *Journal of Geophysical Research: Solid Earth*, *113*(11), 1–16. https://doi.org/10.1029/2008JB005588

Molina, E., Arancibia, G., Sepúlveda, J., Roquer, T., Mery, & D., Morata, D. (2019). Digital Rock Approach to Model the Permeability in an Artificially Heated and Fractured Granodiorite from the Liquiñe Geothermal System (39°S). *Rock Mechanics and Rock Engineering*, in press. https://doi.org/10.1007/s00603-019-01967-6

Moore, D. E., Lockner, D. A., & Byerlee, J. D. (1994). Reduction of permeability in granite at elevated temperatures. *Science*, *265*(5178), 1558–1561. https://doi.org/10.1126/science.265.5178.1558

Munizaga, F., Herve, F., Drake, R., Pankhurst, R. J., Brook, M., & Snelling, N. (1988). Geochronology of the Lake Region of south-central Chile (39°-42°S): Preliminary results. *Journal of South American Earth Sciences*, *1*(3), 309–316.

Muñoz, M. and Hamza, V., 1993. Heat flow and temperature gradients in Chile. *Studia geophysica et geodaetica*, 37(3), pp.315-348.

Nara, Y., Meredith, P. G., Yoneda, T., & Kaneko, K. (2011). Influence of macro-fractures and micro-fractures on permeability and elastic wave velocities in basalt at elevated pressure. *Tectonophysics*, *503*(1–2), 52–59. https://doi.org/10.1016/j.tecto.2010.09.027

Ohno, I. (1995). Temperature Variation of Elastic Properties of α-Quartz up to the α-β transition. *Journal of Physics of the Earth*, *43*(2), 157–169. https://doi.org/10.4294/jpe1952.43.157

Ohno, I., Harada, K., & Yoshitomi, C. (2006). Temperature variation of elastic constants of quartz across the α-β transition. *Physics and Chemistry of Minerals*, *33*(1), 1–9. https://doi.org/10.1007/s00269-005-0008-3

Pankhurst, R. J., Hervé, F., Rojas, L., & Cembrano, J. (1992). Magmatism and tectonics in continental Chiloe, Chile. *Tectonophysics*, *205*, 283–294.

Pankhurst, R. J., Weaver, S. D., Hervé, F., & Larrondo, P. (1999). Mesozoic – Cenozoic evolution of the North Patagonian Batholith in Aysén, southern Chile. *Journal of the Geological Society*, *156*, 673–694. https://doi.org/10.1144/gsjgs.156.4.0673

Passelègue, F. X., Pimienta, L., Faulkner, D., Schubnel, A., Fortin, J., & Guéguen, Y. (2018). Development and Recovery of Stress-Induced Elastic Anisotropy During Cyclic Loading Experiment on Westerly Granite. *Geophysical Research Letters*, *45*, 8156–8166. https://doi.org/10.1029/2018GL078434

Pérez-Flores, P., Veloso, E., Cembrano, J., Sánchez-Alfaro, P., Lizama, M., & Arancibia, G. (2017). Fracture network, fluid pathways and paleostress at the Tolhuaca geothermal field. *Journal of Structural Geology*, *96*, 134–148. https://doi.org/10.1016/j.jsg.2017.01.009

Pérez-Flores, P., Wang, G., Mitchell, T. M., Meredith, P. G., Nara, Y., Sarkar, V., & Cembrano, J. (2017). The effect of offset on fracture permeability of rocks from the Southern Andes Volcanic Zone, Chile. *Journal of Structural Geology*, *104*, 142–158. https://doi.org/10.1016/j.jsg.2017.09.015

Rossenau, M., Melnick, D., & Echtler, H. (2006). Kinematic constraints on intra-arc shear and strain partitioning in the southern Andes between 38°S and 42°S latitude. *Tectonics*, *25*(4). https://doi.org/10.1029/2005TC001943

Sánchez, P., Pérez-Flores, P., Arancibia, G., Cembrano, J., & Reich, M. (2013). Crustal deformation effects on the chemical evolution of geothermal systems: The intra-arc Liquiñe-Ofqui fault system, Southern Andes. *International Geology Review*, *55*(11), 1384–1400. https://doi.org/10.1080/00206814.2013.775731

Schindelin, J., Arganda-Carreras, I., Frise, E., Kaynig, V., Longair, M., Pietzsch, T., Preibisch, S., Rueden, C., Saalfeld, S., Schmidt, B., Tinevez, J. Y., White, D. J., Hartenstein, V., Eliceiri, K., Tomancak, P., & Cardona, A. (2012). Fiji: An open-source platform for biological-image analysis. *Nature Methods*, *9*(7), 676–682. https://doi.org/10.1038/nmeth.2019

Schneider, C. A., Rasband, W. S., & Eliceiri, K. W. (2005). ParaView: An end-User Tool for Large-Data Visualization. *Nature Methods*, *9*(7), 671–675.

Shao, S., Ranjith, P. G., Wasantha, P. L. P., & Chen, B. K. (2015). Experimental and numerical studies on the mechanical behaviour of Australian Strathbogie granite at high temperatures: An application to geothermal energy. *Geothermics*, *54*, 96–108. https://doi.org/10.1016/j.geothermics.2014.11.005

Sibson, R. H. (1996). Structural permeability of fluid-driven fault-fracture meshes. *Journal of Structural Geology*, *18*(8), 1031–1042. https://doi.org/10.1016/0191-8141(96)00032-6

Siegesmund, S., Sousa, L., & Knell, C. (2018). Thermal expansion of granitoids. *Environmental Earth Sciences*, *77*(2), 1–29. https://doi.org/10.1007/s12665-017-7119-2

Stanton-Yonge, A., Griffith, W. A., Cembrano, J., St. Julien, R., & Iturrieta, P. (2016). Tectonic role of margin-parallel and margin-transverse faults during oblique subduction in the Southern Volcanic Zone of the Andes: Insights from Boundary Element Modeling. *Tectonics*, *35*(9), 1990–2013. https://doi.org/10.1002/2016TC004226

Tschumperlé, D., & Deriche, R. (2005). Vector-valued image regularization with PDEs: A common framework for different applications. *IEEE Transactions on Pattern Analysis and Machine Intelligence*, *27*(4), 506–517. https://doi.org/10.1109/TPAMI.2005.87

Tullis, J., & Yund, R. A. (1977). Experimental deformation of dry Westerly granite. *Journal of Geophysical Research*, 82(36), 5705-5718.

UNE-EN 1925. (1999). Métodos de ensayo para piedra natural. Determinación del coeficiente de absorción de agua por capilaridad. AENOR, Madrid

UNE-EN 1926. (2007). Métodos de ensayo para piedra natural. Determinación de la resistencia a la compresión uniaxial. AENOR, Madrid

Vazquez, P., Sánchez-Delgado, N., Carrizo, L., Thomachot-Schneider, C., & Alonso, F. J. (2018). Statistical approach of the influence of petrography in mechanical properties and durability of granitic stones. *Environmental Earth Sciences*, *77*(7), 1–17. https://doi.org/10.1007/s12665-018-7475-6

Vázquez, P., Shushakova, V., & Gómez-Heras, M. (2015). Influence of mineralogy on granite decay induced by temperature increase: Experimental observations and stress simulation. *Engineering Geology*, *189*, 58–67. https://doi.org/10.1016/j.enggeo.2015.01.026

Violay, M., Heap, M. J., Acosta, M., & Madonna, C. (2017). Porosity evolution at the brittle-ductile transition in the continental crust: Implications for deep hydro-geothermal circulation. *Scientific Reports*, *7*(1), 7705.

Wang, X. Q., Schubnel, A., Fortin, J., Guéguen, Y., & Ge, H. K. (2013). Physical properties and brittle strength of thermally cracked granite under confinement. *Journal of Geophysical Research: Solid Earth*, 118(12), 6099-6112.

Yang, S. Q., Ranjith, P. G., Jing, H. W., Tian, W. L., & Ju, Y. (2017). An experimental investigation on thermal damage and failure mechanical behavior of granite after exposure to different high temperature treatments. *Geothermics*, *65*, 180–197. https://doi.org/10.1016/j.geothermics.2016.09.008

Zhao, Z. (2016). Thermal Influence on Mechanical Properties of Granite: A Microcracking Perspective. *Rock Mechanics and Rock Engineering*, *49*(3), 747–762. https://doi.org/10.1007/s00603-015-0767-1

Zhu, W. & Wong, T.-F. (1997) The transition from brittle faulting to cataclastic flow: Permeability evolution. *Journal Geophysical Research, 102*, 3027–3041.

Zhu, S., Zhang, W., Sun, Q., Deng, S., Geng, J., Li, C. 2017. Thermally induced variation of primary wave velocity in granite from Yantai: Experimental and modeling results. *International Journal of Thermal Sciences* 114, 320-326.

Zuo, J.P., Wang, J.T., Sun, Y.J., Chen, Y., Jiang, G.H., Li, Y.H. 2017. Effects of thermal treatment on fracture characteristics of granite from Beishan, a possible high-level radioactive waste disposal site in China. *Engineering Fracture Mechanics* 182, 425-437.